Buoyant miscible viscoplastic injections

M. Faramarzi, S. Akbari, and S. M. Taghavi*
Department of Chemical Engineering, Université Laval, Québec, Québec City, Canada G1V 0A6

(Received 28 February 2024; accepted 24 June 2024; published 15 July 2024)

We experimentally investigate the buoyant miscible injection of a heavy viscoplastic fluid with moderate yield stresses into a lighter Newtonian fluid, via an eccentric inner pipe inside an inclined closed-end outer pipe. To capture the flow dynamics, we employ nonintrusive methods, including camera imaging and ultrasound Doppler velocimetry. Our analysis reveals that the flow behavior is governed by a set of dimensionless flow parameters: Reynolds number, Froude number, inclination angle, Bingham number, and viscosity ratio. Using a dimensionless plane that elegantly combines the aforementioned dimensionless numbers, we successfully identify and categorize various flow regimes, such as stable and unstable slumping, separation, and diffusive and nondiffusive mixing. We analyze these flow regimes and quantify their transition boundaries. Our analysis also considers the distinct characteristics of these flow regimes, focusing on interfacial velocities, including the heavy fluid front velocity, the separated piece velocity, and the backflow front velocity, and examines the flow velocity field and mixing index.

DOI: 10.1103/PhysRevFluids.9.073301

I. INTRODUCTION

Injection flows are prevalent in diverse industrial applications and they are widely studied in microfluidic systems and biomedical contexts [1–3], cleaning processes [4,5], food processing operations [6,7], coating and printing devices [8,9], carbon geosequestrations [10–12], as well as the oil and gas industries [13–15]. Viscoplastic fluids used in coating, 3D printing [16–20], oil and gas well plug and abandonment (P&A) [21,22], and microfluidics [23] offer stability in injection processes but they also introduce complexities in terms of their rheology and flow studies [24]. In particular, analyzing their use in confined geometries requires an understanding of the fluid interface dynamics and yielding behavior [25,26]. The complexity of injection flows involving viscoplastic fluids also arises from a wide range of flow parameters involved, such as fluid properties, geometry, and operational parameters, all influencing flow patterns and regimes. To better understand these challenges and the dynamics of such flows, in this work, we experimentally study the buoyant miscible injection of a heavy viscoplastic fluid (at moderate yield stresses) into an inclined closed-end pipe filled with a light Newtonian fluid, and explore various flow regimes.

Studies on viscoplastic fluid extrusions into passive fluids have revealed some key dynamics. For example, Coussot and Gaulard [27] found that, when injected into air, viscoplastic fluids initially form an unyielded layer, which eventually yields and breaks upon exceeding the yield stress, with the broken filament length increasing with the flow rate. Balmforth *et al.* [28,29] developed a model to describe instability growth and pinch-off in these fluids, noting that increasing the yield stress leads to larger broken filament volumes, shorter necks, squatter end cones, and higher pinch points. Aytouna *et al.* [30] observed that, at low flow rates, viscoplastic fluids exhibit a dripping regime similar to Newtonian fluids. Further studies [31–33] have investigated droplet injections into passive

*Contact author: seyed-mohammad.taghavi@gch.ulaval.ca

fluids without confinement. Moreover, research on the interplay between capillary and yield stresses in viscoplastic droplet spreading is detailed in the works by Jalaal, Zhang, and others [18,34–36], extending beyond the purview of our current research.

Research on the impact of the yield stress on viscoplastic fluid injections has explored various aspects, particularly for fluids at moderate yield stresses. For instance, Saidi *et al.* [37] studied the spreading of yield stress fluid drops on solid surfaces, revealing that relatively smaller yield stress gels form nearly spherical drops. Amiri *et al.* [38] investigated the injection of a heavier Newtonian fluid into a lighter yield stress fluid in a vertical pipe, finding high instability and significant fluid mixing at low yield stresses, due to the dominance of buoyancy forces. Hassanzadeh *et al.* [39] examined neutrally buoyant Newtonian jets in viscoplastic ambient fluids across a wide yield stress range, identifying four flow regimes (as the yield stress progressively increases): mixing, mushroom, fingering, and fracturing. They noted that low-yield stress fluids exhibit notable instability and mixing at high injection velocities, transitioning to clearer fluid boundaries and reduced mixing as the yield stress increases. Using experiments and modeling, Akbari and Taghavi [22] studied the buoyant miscible injection of a heavy viscoplastic fluid with high-yield stresses into a lighter Newtonian fluid, in a vertically closed-end pipe. They identified three main flow regimes: breakup, coiling, and buckling (bulging). Further exploration into long-term flow characteristics led to the identification of various subregimes, including regular, irregular, and free-coiling behaviors, breakup with and without satellite drops, and bulging with and without subsequent falling parts [40].

A common flow feature in buoyant injection and displacement flows is the slumping pattern, particularly seen in inclined geometries, i.e., when the heavy fluid slumps underneath the light fluid. Lyu and Taghavi [41,42] observed slumping displacements, predominantly at near-horizontal inclinations, during the buoyant miscible displacement of a light viscoplastic fluid by a heavier Newtonian one in an inclined pipe. They attributed slumping not only to inclination but also to instances where the yield stress becomes comparable with inertia and buoyant stresses, resulting in decreased interfacial instabilities and a sharp fluid interface. Renteria and Frigaard [43] found a similar slumping regime in an eccentric annulus, when buoyant stresses are positive and sufficient to overcome the impacts of eccentricity. Considering buoyant displacements involving Newtonian and shear-thinning fluids, Mollaabbasi *et al.* [44] observed slumping-type flow patterns in horizontal to near-horizontal inclinations. Further studies [45–50] have explored slumping patterns in various flow configurations, including confined geometries, dam-breaks, thin film flows, and turbidity currents.

The injection rate is a critical factor in fluid injections and displacements, significantly influencing the flow dynamics and mixing quality. Sher and Wood [51] found in their study on buoyant iso-viscous fluid injections in a horizontal channel that higher flow rates enhance mixing near the injection inlet, affecting the overall flow structure. In their Newtonian displacements, Taghavi *et al.* [52] and Alba *et al.* [53] observed that low injection rates lead to Kelvin Helmholtz instabilities, while increased injection rates may counterintuitively stabilize the flow and linearly increase the displacement front velocity. However, at high injection rates, the flow becomes unstable and mixing remains efficient due to the diffusive nature of the flow. Amiri *et al.* [54] identified two flow regimes (stable and unstable) in buoyant displacement flows of two miscible isoviscous Newtonian fluids in a vertical pipe, associating stable flows with segregated interfaces and unstable ones with interfacial instabilities and front detachment. Regarding injection flows in a closed-end pipe, Akbari and Taghavi [13,22,40,55,56] also highlighted that the injection rate primarily affects the initial flow stages (typically near the injection inlet) in buoyant injection flows with Newtonian and non-Newtonian fluids.

Buoyant stresses, caused by the density difference between the injected and *in situ* fluids, significantly influence buoyant injection flows. Previous research indicates that a greater density difference enhances velocity gradients, potentially leading to Kelvin-Helmholtz instabilities and a shift towards turbulent and diffusive regimes [53,57–60]. In addition, increasing the inclination angle towards the vertical enhances axial buoyant stresses, which may cause interfacial instabilities and increase mixing, as demonstrated in several numerical and experimental studies [44,57,61].

From a practical point of view, our research is motivated by processes involved in the P&A operations of oil and gas wells, particularly those focusing on cement plug placement techniques, such as the dump-bailing method. This method is extensively used for protecting water aquifers and the environment from reservoir fluid leaks [21,62]. In this method, cement slurry is a water-based fluid containing approximately 70% water, with additives such as cement powder and retarders [21]. The wellbore fluid is typically water (or salt water), making it miscible with the cement slurry. This presents a challenge in the dump-bailing method, as the properties of the in-place wellbore fluid can directly influence the flow dynamics and, eventually, the physical and chemical properties of the injected cement. The execution of the dump-bailing method involves injecting a heavy viscoplastic cement slurry with moderate yield stresses through an eccentric inner pipe into a casing (i.e., circular pipe); the cement slurry is designed to displace and remove light *in situ* Newtonian fluids (usually water) to eventually seal the wellbore effectively, thus, preventing oil and gas migrations [13,21,62,63]. In this context, previous studies, e.g., Akbari and Taghavi [22], have focused on structured flows in buoyant viscoplastic injections with high-yield stresses, while our study considers moderate yield stresses. At high-yield stress fluids typically show structured flow with considerable unyielded regions and a sharp interface [22,40], while moderate yield stress fluids exhibit unstructured or semistructured flow, gradually yielding over time, leading in largely yielded viscoplastic fluid regions, and causing instabilities and mixing at the interface. This is relevant to dump-bailing, where cement slurry yield stress values are not very high and mixing and instabilities are expected, making our study crucial for realistic industrial applications with significant practical implications.

Our study addresses a gap in buoyant miscible viscoplastic fluid injection research. While previous work has focused on viscoplastic fluid injections into dynamically passive [28–30] and dynamically active fluids [22,40], little research exists on largely yielded viscoplastic fluids, particularly in inclined orientations. In this context, a dynamically passive fluid remains stagnant, while a dynamically active fluid directly contacts the injected fluid and applies significant forces that alter the flow dynamics. Our research experimentally explores buoyant miscible viscoplastic fluid injections at moderate yield stresses into a dynamically active Newtonian surrounding fluid, via an eccentric inner pipe inside an inclined closed-end outer pipe. Our pair of fluids consists of water and a viscoplastic fluid made from a Carbopol solution and is considered miscible with no significant surface tension effects in line with recent studies [39,40,64–68]. Our study also falls into the category of high Péclet number, where the two fluids approach the immiscible limit with zero surface tension (see, for example, Refs. [69,70]). We offer an in-depth analysis of flow regimes and interfacial flow characteristics using dimensionless parameters governing flow dynamics.

The manuscript is structured as follows: Section II details the experimental setup, procedure, fluid preparation, rheometry, and experiment scope. Section III presents results and discussion, starting with an overview of the flow regimes observed (Sec. III A), followed by the classification of these regimes on dimensional and dimensionless planes and regime transitions (Sec. III B). The manuscript then explores interfacial velocities in viscoplastic injection flows (Sec. III C), examines the velocity field across different flow regimes (Sec. III D), and evaluates fluid displacement quality through a mixing index (Sec. III E). Finally, Sec. IV concludes the manuscript with a summary.

II. EXPERIMENTS

In this section, we outline our experimental setup and procedure, as well as measuring equipment. Then, we describe how we prepare our viscoplastic fluids and how we conduct their rheometry. Finally, we present the key governing parameters in dimensional and dimensionless forms, along with their respective ranges within our experiments.

A. Experimental setup and procedure

Motivated by the industrial dump-bailing method in P&A applications, we constructed a scaled-down experimental setup consisting of two transparent pipes (see Figure 1). The outer pipe has an

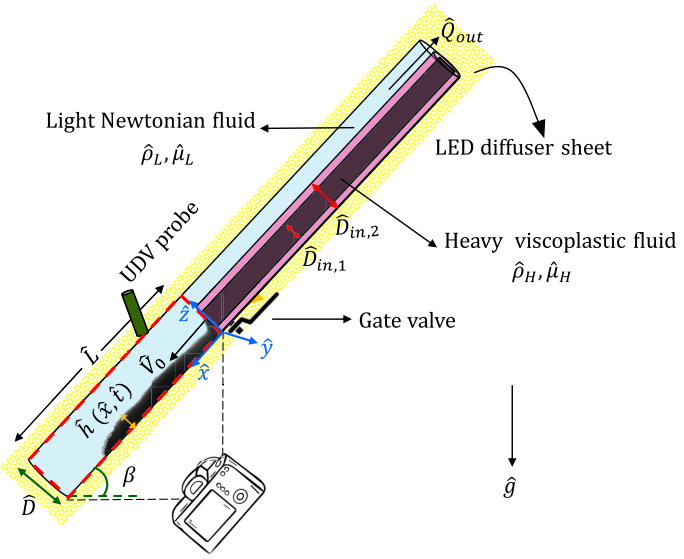

FIG. 1. Schematic view of the experimental setup. The red dashed line represents the domain of study.

inner diameter of 3.81 (cm) and is 2.46 (m) long. The inner one is also 2 (m) long, with inner and outer diameters of 1.27 (cm) and 2.54 (cm), respectively. The length of the outer pipe is sufficiently large so that the outlet area located at the top of the pipe does not exert any influence on the flow characteristics. Considering P&A applications, an eccentric configuration is adjusted by placing the inner pipe inside the closed-end outer one. The inner pipe is connected to a gear pump (Ismatech 405A) to deliver the viscoplastic fluid at a flow rate that is precisely measured. The setup is affixed to a rotating support structure, enabling a range of inclinations from horizontal to vertical orientations. A gate valve is installed at the end of the inner pipe to segregate the injected and *in situ* fluids, before beginning an experiment.

The preparation for an experiment includes filling the outer pipe with transparent deionized water (as a light Newtonian fluid). The inner pipe is then filled with a heavy viscoplastic fluid. For visualization, this viscoplastic fluid is colored with ink (Fountain Pen India black) at a concentration of 0.8 (g/l) in deionized water, mixed using a three-blade stirrer to create a homogeneous solution. This small amount of ink concentration has a negligible effect on the solution's rheology [40] and serves as an ideal tracer for visualization purposes [38,39,54,64,67].

Before running an experiment, the flow rate is adjusted using a pump device. Once the gate valve positioned at the lower end of the inner pipe is opened, the heavy viscoplastic fluid is injected into the outer pipe. Continuous injection results in the movement of the light fluid toward the annulus section, and it eventually exits the setup through the outlet area. In all experiments, a flow meter (FTB-421, Omega) with an accuracy of $\pm 3\%$ measures the flow rate, in addition to measurements recorded by the pump for verifications. Moreover, a black-and-white digital camera (Basler acA2040) with a resolution of 4.2 megapixels and a typical frame rate of 90 frames per second captures the injection flow process.

Light-emitting diodes are put behind the pipe, with diffusive panels in between, to ensure equal lighting over the pipe. Light absorption calibrations are conducted using established procedures. In particular, before each experiment, images of the pipe filled with the transparent and dark fluids are captured separately. According to the Beer-Lambert law [55,71], these images are considered as references for light intensities, allowing for the determination of normalized concentration fields. The collected images are processed using a custom image processing MATLAB code to extract relevant flow details.

A nonintrusive ultrasound Doppler velocimetry (UDV) method is used to obtain local axial velocity profiles. The UDV approach determines velocity profiles by monitoring the difference in frequency between a transmitted sound wave and its echo. The UDV measurements in this study are conducted below the gate valve, with the UDV probe positioned on the upper wall of the pipe (see Figure 1). Seeding particles, in the form of copolyamide particles with an average size of 60 (μm), are introduced into both the *in situ* and injected fluids, at an established volumetric concentration of 0.2 (g/l). These fluids are mixed for 4 h using a mixer operating at 400 (rpm). To achieve an accurate signal-to-noise ratio, the UDV probe (DOP4000, Signal Processing S.A.) is positioned at a 75-degree angle relative to the pipe's axis [55,56].

B. Fluid preparation and rheometry

The injection fluid is prepared by combining deionized water with Carbopol powder (Carbomer 940 from Making Cosmetics Co.). To create various injection fluids with varying yield stresses, different concentrations of Carbopol powders are considered. In addition, to enhance fluid flow visibility and have injection fluid with different densities, the previously mentioned black ink and special fine-granulated sugar are, respectively, added to the fluid, before mixing it with the Carbopol powder. In the meantime, the fluid's density is controlled using a high-accuracy density meter (Anton Paar DMA 35).

The procedure for preparing our viscoplastic fluids involves the gradual addition of Carbopol powder to the dyed deionized water. To achieve a homogeneous mixture, the solution is mixed at high speed [360 (rpm)] for 1 h using a mixer (IKA Werke Eurostat Power). Then, the mixture is allowed to rest for 24 h to eliminate bubbles and achieve a bubble-free state. Since the addition of Carbopol powder results in an acidic solution, with a pH ranging from 3 to 5 and with no yield stress, the solution is neutralized to pH = 7 by adding an appropriate amount of sodium hydroxide (i.e., typically 0.29 g of NaOH (Fisher BioReagents) per 1 g of Carbopol powder). Finally, the solution is centrifuged at 360 (rpm) for 1 h to complete its preparation.

The rheological measurements of the injection fluid (Carbopol solution) are conducted utilizing a DHR-3 rheometer from TA Instruments. The tests are carried out with a parallel-plate geometry, featuring a 40 (mm) diameter and a mean gap of 1 (mm). To reduce the effects of wall slip during the measurements performed at low shear rates, sandpapers (as rough surfaces) are affixed to the rheometer plates [72,73].

Steady-state flow curves of viscoplastic solutions are derived through controlled shear rate ($\hat{\dot{\gamma}}$) experiments, where the samples are subjected to shearing within an ascending range of $10^{-1} < \hat{\dot{\gamma}} < 10^{3}$ (s^{-1}) as illustrated in Figure 2(a). The symbols within the figure denote the rheometry data, while the solid lines represent the fitted Herschel-Bulkley (H-B) model, which is defined as

$$\begin{aligned} \hat{\dot{\gamma}} &= 0, && |\,\hat{\tau}\,| \leqslant \hat{\tau}_y, \\ \hat{\tau} &= \hat{\tau}_y + \hat{\kappa}\hat{\dot{\gamma}}^n, && |\,\hat{\tau}\,| > \hat{\tau}_y, \end{aligned} \tag{1}$$

in which $\hat{\tau}$ is the shear stress, $\hat{\kappa}$ is the consistency index, and n is the power-law index. Accordingly, the characteristic viscosity of the heavy viscoplastic fluid ($\hat{\mu}_H$) is defined as

$$\hat{\mu}_H = \hat{\tau}_y \hat{\dot{\gamma}}_c^{-1} + \hat{\kappa}\hat{\dot{\gamma}}_c^{n-1}, \tag{2}$$

in which the characteristic shear rate is defied as $\hat{\dot{\gamma}}_c = \hat{V}_0/\hat{D}$, with $\hat{V}_0$ and $\hat{D}$ being the mean injection velocity and the inner diameter of the outer pipe, respectively.

Carbopol rheological data points can be fitted with lines corresponding to the H-B model parameters, as also reported in other works, e.g., Jaworski *et al.* [74]. Figure 2(a) presents the flow curves for some Carbopol solutions. In this figure, the color of the H-B model applied to each solution also aligns with the corresponding rheometry data. The color spectrum transitions from lighter to darker gradients represent the variation in the yield stress values (darker colors indicate higher yield stresses). As illustrated in Figure 2(a), the flow curves present the material characteristics beyond the critical stress, where the samples exhibit shear-thinning behavior. In

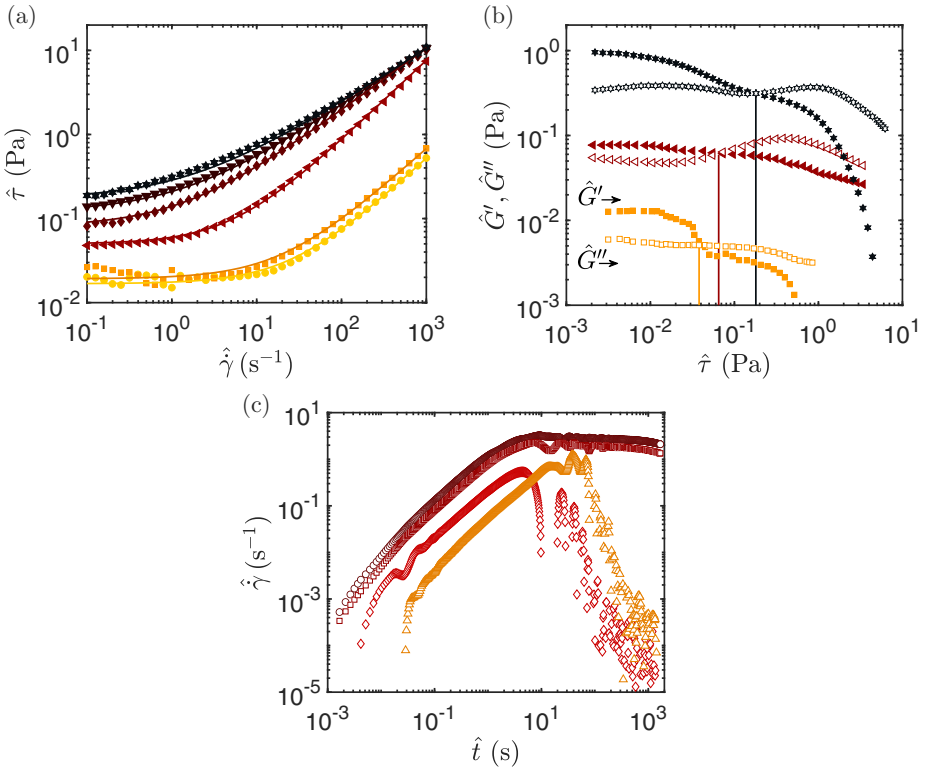

FIG. 2. (a) Flow curves for Samples I (●), II (■), VI (◀), VII (◆), VIII (▼), IX (★) showing shear stress ($\hat{\tau}$) versus shear rate ($\hat{\dot{\gamma}}$). Lines, color-matched to symbols, represent Herschel-Bulkley fits (Eq. (1)) from Table I, with darker shades indicating higher $\hat{\tau}_y$. (b) Oscillation amplitude sweep results for Samples II (■, □), VI (◀, ◁), IX (★, ✡) showing storage modulus ($\hat{G}'$) and loss modulus ($\hat{G}''$) as filled and hollow symbols, respectively. Yield stress ($\hat{\tau}_y$) is marked by vertical lines at $\hat{G}'$ and $\hat{G}''$ crossover points. (c) Creep tests for Sample V using stress values 0.005 (triangles), 0.01 (diamonds), 0.1 (squares), 0.15 (circles) (Pa), with symbol darkness indicating stress level.

lower shear rates, the shear stress converges to a specific value, called the yield stress ($\hat{\tau}_y$) [26,75]. The small fluctuations in the flow curves at low shear rates may result from the inertial effect of the rheometer [76,77]. Table I lists the characteristics of our Carbopol solutions, including the rheological parameters determined using the H-B model, as well as the fluid densities.

As a complementary rheological characterization, oscillatory rheometry tests are also carried out, to characterize the elastic and viscous behaviors of the prepared Carbopol solutions at a fixed frequency of 1 (Hz), with the applied oscillation stress ranging from 10^{-3} to 10^{1} (Pa). This makes it possible to assess the storage modulus ($\hat{G}'$) and loss modulus ($\hat{G}''$), representing the elastic and viscous properties, respectively. Figure 2(b) shows the results of the oscillation amplitude sweep tests for Samples II, V, VI, and IX. At low stress levels ($\hat{\tau}$), all sample solutions show $\hat{G}'$ (elastic modulus) exceeding $\hat{G}''$ (loss modulus), indicating a solid-like behavior pre-yielding [39,75,78]. However, under high shear stresses, the material's viscous behavior overtakes its elastic properties, with both $\hat{G}'$ and $\hat{G}''$ decreasing at varying rates as $\hat{\tau}$ increases, leading to a dominance of $\hat{G}''$ over $\hat{G}'$, signifying flow and minimal elastic effects.

The vertical lines in Figure 2(b) show the stress values where the $\hat{G}'$ and $\hat{G}''$ curves cross over, suggesting a rough estimation of the yield stress [75,78–81]. Nevertheless, it is crucial to use caution when predicting the yield point using this crossover method [82,83]. The crossover method

TABLE I. Characteristics of different Carbopol solutions used in this study. Rheological parameters were obtained by fitting shear stress-shear rate curves to the H-B model, including the yield stress ($\hat{\tau}_y$), consistency index ($\hat{\kappa}$), and power-law index (n). The last column shows the density corresponding to each sample.

Sample	$\hat{\tau}_y$ (Pa)	$\hat{\kappa}$ (Pa.s^n)	n	$\hat{\rho}_H$ (kg/m^3)
I	0.017	0.0008	0.94	1004
II	0.019	0.001	0.91	1004
III	0.02	0.11	0.64	1016
IV	0.032	0.055	0.75	1018
V	0.04	0.11	0.7	1004
VI	0.05	0.01	0.96	1004
VII	0.08	0.06	0.75	999
VIII	0.12	0.09	0.69	1015
IX	0.17	0.12	0.65	1036

would suggest yield stresses of 0.035 (Pa), 0.065 (Pa), and 0.18 (Pa) for Samples II, VI, and IX, respectively. However, these values calculated at the crossing of the $\hat{G}'$ and $\hat{G}''$ curves slightly differ from those obtained from the H-B model fitting in Figure 2(a). This aligns with recent rheology measurements of different viscoplastic fluids [66,82].

Figure 2(c) shows the results of our creep tests for a given Carbopol solution (Sample V), by applying a constant shear stress and measuring the shear rate as a function of time. As observed, when the shear stress values are $\hat{\tau} = 0.005\,(\text{Pa})$ and $\hat{\tau} = 0.01\,(\text{Pa})$, the corresponding shear rate decreases to nearly zero, over an extended duration. This behavior indicates that the applied stress falls below the yield stress, denoted as $\hat{\tau}_y = 0.04\,(\text{Pa})$ for Sample V, as indicated in Figure 2(a) and Table I. However, when the shear stress is $\hat{\tau} = 0.1\,(\text{Pa})$ and $\hat{\tau} = 0.15\,(\text{Pa})$, the shear rate remains constant at a nonzero value. This finding also generally aligns with earlier observations and rheological measurements [22,84].

To ensure precise measurements across the range of yield stress values in this study, most rheological tests were repeated multiple times. Also, oscillatory rheometry and creep tests confirmed that our prepared fluid samples possess yield stress. In addition, several rheological models, including the power law model, were evaluated to identify the most accurate one. Based on this, the H-B model was found to provide the most accurate results, consistent with previous studies using Carbopol powder and similar fluid preparations within the yield stress range determined in this study [38,39,68,85–88].

C. Scope of experiments

Our experiments, as shown in Table II, involve 12 dimensional parameters influencing the fluid flow, leading to 9 dimensionless numbers based on Buckingham's π-theorem. In addition, the power-law index (n) and inclination angle (β) are two more dimensionless parameters, totaling 11 key dimensionless numbers governing the injection flow problem (Table III). To derive these dimensionless numbers, characteristic parameters such as the diameter ($\hat{D}$), velocity ($\hat{V}_0$), combined viscosity ($\sqrt{\hat{\mu}_H \hat{\mu}_L}$), average density ($\frac{(\hat{\rho}_H + \hat{\rho}_L)}{2}$), diffusion coefficient ($\hat{D}_m$), and yield stress ($\hat{\tau}_y$) are employed.

Our analysis can be made feasible by employing some assumptions and simplifications to decrease the quantity of the key dimensionless numbers. For example, we consider constant values for some dimensionless numbers and geometrical parameters, such as the diameter ratios (DR_1, DR_2) and the aspect ratio (δ). The Atwood number (At), representing negligible density difference ($At \ll 1$), is also excluded, while density differences are still captured by the Froude number (Fr). With a high Péclet number ($Pe \gg 1$), molecular diffusion itself is insignificant in our experiments, as our fluids do not mix due to molecular mixing within our experimental timescale. Moreover, previous research has demonstrated that the molecular diffusion coefficient in polymer solutions

TABLE II. Ranges of dimensional parameters in our experiments. The hat symbol is consistently used for denoting dimensional parameters throughout the manuscript.

Parameter	Name	Range or value
$\hat{D}$	Inner diameter of outer pipe	3.81 (cm)
$\hat{D}_{\text{in},1}$	Inner diameter of inner pipe	1.27 (cm)
$\hat{D}_{\text{in},2}$	Outer diameter of inner pipe	2.54 (cm)
$\hat{\rho}_H$	Heavy fluid density	999–1036 (kg/m^3)
$\hat{\rho}_L$	Light fluid density	998 (kg/m^3)
$\hat{\mu}_L$	Light fluid viscosity	0.001 (Pa s)
$\hat{\mu}_H$	Heavy fluid viscosity	0.003–0.830 (Pa s)
$\hat{L}$	Length of flow domain	46 (cm)
$\hat{V}_0$	Mean injection velocity	10–329 (mm/s)
$\hat{g}$	Gravitational acceleration	9.81 (m/s^2)
$\hat{D}_m$	Molecular diffusivity	$\sim 10^{-9}$ (m^2/s)
$\hat{\tau}_y$	Yield stress of the heavy fluid	0.017–0.170 (Pa)
$\hat{\kappa}$	Consistency index of the heavy fluid	0.0008–0.1200 (Pa s^n)

is either lower than or comparable to that in pure water, and it remains unaffected by shear rate [89]. Hence, it is reasonable to assume that the molecular diffusivity between water and Carbopol solutions is small, leading us to expect a minimal effect of molecular diffusion on our findings. Also, although the power-law index (n) varies between 0.64 and 0.96, it has a low standard deviation of 0.11 around the mean of 0.78, indicating most experiments are within $n = 0.78 \pm 0.11$. Nonetheless, n remains crucial for defining the viscosity ratio:

$$M = \frac{\hat{\mu}_L}{\sqrt{\hat{\mu}_H \hat{\mu}_L}} = \left(\frac{\hat{\mu}_L}{\hat{\tau}_y \left(\frac{\hat{V}_0}{\hat{D}}\right)^{-1} + \hat{\kappa} \left(\frac{\hat{V}_0}{\hat{D}}\right)^{n-1}} \right)^{1/2}. \tag{3}$$

Considering the above-stated assumptions and simplifications, in general, our flows are effectively described using five dimensionless numbers or their combinations: Reynolds number (Re),

TABLE III. Dimensionless parameters and their corresponding ranges in our study.

Parameter	Name	Definition	Range
δ	Aspect ratio	$\hat{L}/\hat{D}$	12.07
DR_1	Diameter ratio 1	$\hat{D}_{\text{in},1}/\hat{D}$	0.34
DR_2	Diameter ratio 2	$\hat{D}_{\text{in},2}/\hat{D}$	0.67
Re	Reynolds number	$\frac{(\hat{\rho}_H+\hat{\rho}_L)\hat{V}_0\hat{D}}{2\sqrt{\hat{\mu}_L\hat{\mu}_H}}$	13–7034
At	Atwood number	$\frac{\hat{\rho}_H-\hat{\rho}_L}{\hat{\rho}_H+\hat{\rho}_L}$	0.0005–0.019
Fr	Froude number	$\frac{\hat{V}_0}{\sqrt{At\hat{g}\hat{D}}}$	0.12–17.3
B	Bingham number	$\frac{\hat{\tau}_y\hat{D}}{\sqrt{\hat{\mu}_H\hat{\mu}_L}\hat{V}_0}$	0.41–22.4
Pe	Péclet number	$\frac{\hat{V}_0\hat{D}}{\hat{D}_m}$	10^5–10^7
M	Viscosity ratio	$\sqrt{\frac{\hat{\mu}_L}{\hat{\mu}_H}}$	0.03–0.6
n	Power-law index	—	0.64–0.96
β	Inclination angle	From horizontal	5–90°

Froude number (Fr), Bingham number (B), viscosity ratio (M), and inclination angle (β). Re measures the balance between inertial and viscous forces, varying from $O(10)$ to $O(10^3)$. Fr assesses inertial versus buoyant stresses, ranging from $O(10^{-1})$ to $O(10)$. Also, B quantifies the interplay between yield and viscous stresses, spanning $O(10^{-1})$ to $O(10)$. M falls within $O(10^{-2})$ to $O(10^{-1})$, and β covers inclinations from nearly horizontal to vertical.

By considering a balance between the characteristic longitudinal buoyant stress and the characteristic viscous stress, a dimensionless buoyancy number can be also derived (as a practical quantity):

$$(\hat{\rho}_H - \hat{\rho}_L)\hat{g}\hat{D}\sin(\beta) \sim \sqrt{\hat{\mu}_H\hat{\mu}_L}\frac{\hat{V}_0}{\hat{D}} \Rightarrow \chi = \frac{(\hat{\rho}_H - \hat{\rho}_L)\hat{g}\hat{D}^2\sin(\beta)}{\sqrt{\hat{\mu}_H\hat{\mu}_L}\hat{V}_0}, \tag{4}$$

which effectively combines Re, Fr, and β in the form of

$$\chi \equiv \frac{2\mathrm{Re}}{\mathrm{Fr}^2}\sin(\beta). \tag{5}$$

Prior to moving on to the results section, to facilitate the generalization of our findings in what follows, it is crucial to mention that the lengths, velocities, and time will be made dimensionless by dividing them with $\hat{D}$, $\hat{V}_0$, and $\hat{D}/\hat{V}_0$, respectively.

A few remarks and clarifications

Our *in situ* fluid (deionized water) is a Newtonian fluid, while the injected fluid (Carbopol gel) is a non-Newtonian viscoplastic fluid. The Carbopol gel, containing less than 0.05% (wt./wt.) Carbopol powder and sodium hydroxide (NaOH), is formed by adding NaOH to a mixture of deionized water and Carbopol powder, resulting in a homogeneous viscoplastic gel. Also, rheological measurements confirm that the viscoplastic solutions differ from the *in situ* fluid in both rheological properties and density. Therefore, our injection fluid experiments deal with two fluids.

In our work, Carbopol solutions and water are considered miscible with no surface tension effects, as recent studies show that the surface tension for such fluids is minimal across varying Carbopol concentrations [90,91]. This also aligns with recent studies treating such fluids as miscible [64–67]. Considering this in our flow, the time scale for molecular diffusivity is around $\hat{D}^2/\hat{D}_m \approx 10^5$ (s), while each experiment lasts about 10^2 (s). Therefore, we have $\mathrm{Pe} \gg 10^6$ in our laboratory flows (and their corresponding industrial-scale flows), meaning that initially separated fluids should exhibit sharp interfaces limited to thin interfacial layers of dimensionless size $\mathrm{Pe}^{-1/2}$ over experimental time scales. In fact, previous studies, e.g., the classical works of Refs. [69,70], have shown that displacement flows at high Pe approach their zero surface tension immiscible limit, with a sharp, stable interface. However, this would be only valid in the absence of hydrodynamic effects such as instability, mixing, and dispersion. In fact, in our injection flows, such hydrodynamic effects are present and can indeed result in mixing between the fluids involved. For instance, large velocity field variations and local turbulent flows may be expected to further facilitate mixing by advecting mixed volumes in the flow domain.

We assume that the inner diameter of the outer pipe is the dominant length scale in our system, given that the displacement flow and observed regimes primarily occur within it. This choice aligns with the literature, where studies employing a partial inlet injection configuration within confined pipes [22,92], as well as those investigating core annular flows [93–95]. However, in unconfined or unbounded mediums such as injection or jet flows in large boxes, the diameters of injection inlets are typically considered a dominant parameter [39,96,97]. Nonetheless, in our case, using the inner diameter of the inner pipe to define the characteristic shear rate would result in Pe and B that remain relatively unchanged, while Re would be nearly halved, and Fr would approximately double.

As discussed in the Introduction, previous studies have mainly focused on structured flows in buoyant viscoplastic injections with high-yield stresses, whereas this work focuses on moderate yield stresses. While the former results in structured flows with unyielded regions and a sharp interface, the latter leads to largely yielded flows, with instabilities, and mixing at the interface,

depending also on the other forces, such as buoyancy, viscosity, inertia, etc. In this context, the Newtonian Bingham number ($B_N = \frac{B}{M}$), representing the ratio of the viscoplastic fluid's yield stress to the in-place Newtonian fluid's viscous stress, is commonly used to distinguish between structured and unstructured flows, thereby differentiating between large and moderate yield stress flows. Prior research, e.g., Refs. [22,40], has focused on large B_N up to $B_N \approx 10^5$ (i.e., large yield stresses), demonstrating that viscoplastic injection flows are predominantly structured with $B_N \gtrsim 10^3$. Our study, however, investigates $B_N \lesssim 10^3$ i.e., revealing unstructured flows, which is indicative of moderate yield stresses.

III. RESULTS AND DISCUSSION

This section presents an overview of various flow regimes observed in our experiments, transitions between different regimes on a dimensionless plane, interfacial velocities in our viscoplastic injection flows, velocity field of different flow regimes, and, finally, fluid displacement quality using a proposed mixing index.

A. General observation

This section presents general observations over 120 experiments covering a wide range of experimental parameters, including injection velocities, inclination angles, density differences, and rheological parameters. When a heavy viscoplastic fluid is injected from the inner pipe into a light Newtonian fluid, an interfacial flow develops in the pipe, the heavy fluid front gradually approaches the pipe end, and at long times the heavy fluid eventually fills the pipe section below the injection inlet. Figure 3 depicts four distinct flow regimes that arise during the advancement and interaction of the viscoplastic fluid with the Newtonian fluid in our experiments:

1. Stable slumping regime

Figure 3(a) depicts the snapshots of a typical experiment in this regime. The stable slumping flow regime is more common at low to moderate inclination angles, small density differences, low injection rates, and relatively larger yield stresses. In this regime, as a heavy viscoplastic fluid is injected into the flow domain, it initially generates a buoyant jet. However, soon afterwards, the heavy viscoplastic fluid slumps underneath the light *in situ* Newtonian fluid. The stable slumping pattern progresses towards the pipe end, typically maintaining a nearly constant front velocity and a uniform height of the heavy fluid front. Upon reaching the pipe end, the front of the heavy viscoplastic fluid strikes the end wall, rises, and reverses to advance in the opposite direction to that of the injection. The returning front moves toward the outlet boundary, while the injected heavy viscoplastic fluid continues to flow along the lower wall of the pipe, effectively displacing the light Newtonian fluid.

2. Unstable slumping regime

Figure 3(b) displays the snapshots corresponding to this flow regime. The unstable slumping regime is typically observed when the injection rate is high, at low to moderate inclination angles, small density differences, and relatively larger yield stresses. In this flow regime, the injection of the heavy viscoplastic fluid initially creates a noticeable buoyant jet, resulting in a mixing region (i.e., a mixture of the injected and *in situ* fluids), which subsequently develops near the injection inlet, covering the pipe transverse direction. This observation aligns with previous studies on miscible displacement flows [51,53,54]. In such cases, interfacial instabilities and the development of mixing regions near the inlet tend to increase with increasing the injection velocities. Once the mixing zone is sufficiently extended, the heavy viscoplastic fluid begins to slump underneath the *in situ* Newtonian fluid, moves towards the pipe end, hits the end wall, and then returns toward the outlet boundary. While some portion of the initially injected heavy viscoplastic fluid continues to flow

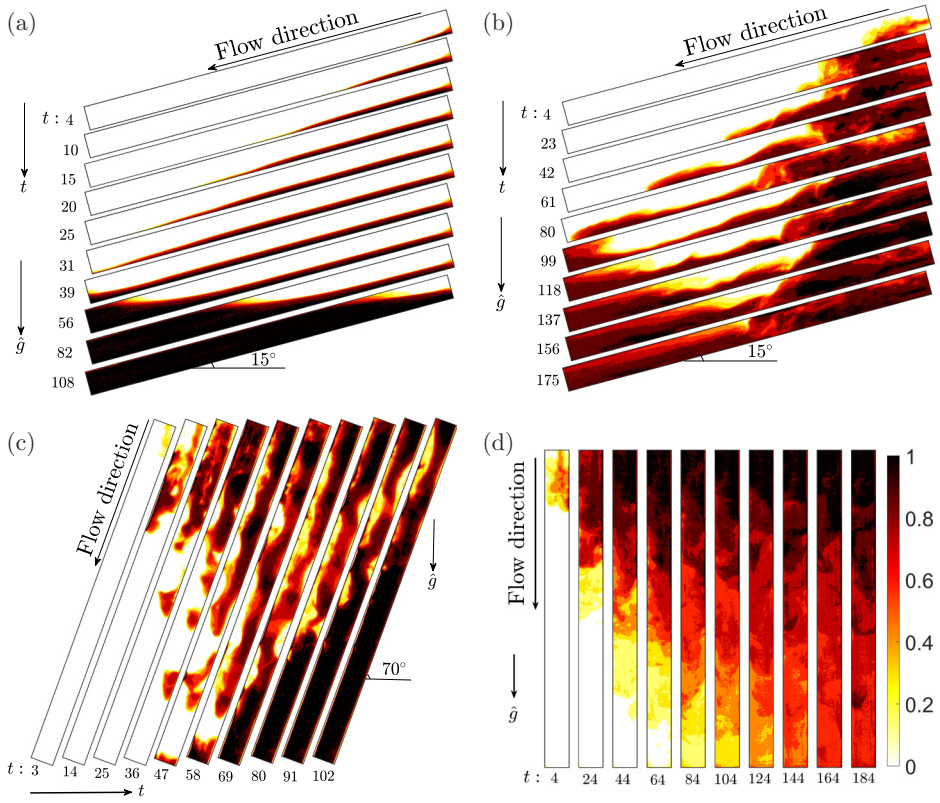

FIG. 3. (a) Snapshots for an experiment within the stable slumping regime with Re = 56, $M = 0.09$, $B = 10.3$, $\beta = 15^\circ$, and Fr = 0.49. (b) Snapshots for an experiment within the unstable slumping regime with Re = 2606, $M = 0.42$, $B = 1.91$, $\beta = 15^\circ$, and Fr = 4.8. (c) Snapshots for an experiment within the separation regime with Re = 418, $B = 1.46$, $M = 0.1$ $\beta = 70^\circ$, and Fr = 3.2. (d) Snapshots for an experiment within the mixing regime with Re = 701, $B = 0.58$, $M = 0.12$, $\beta = 90^\circ$, and Fr = 2.67. The colorbar corresponds to the concentration of the heavy fluid in all panels. All snapshots include dimensionless experiment times beside each image and a dimensionless field of view of 1×12, here and throughout the manuscript.

along the lower wall of the pipe, unlike the stable slumping regime, other flow portions are diverted directly toward the outlet, due to the presence of a mixing zone near the injection inlet.

3. Separation regime

Figure 3(c) illustrates a typical experimental image sequence of this flow regime, which is usually observed at high inclination angles, large density differences along with large yield stresses, and small to moderate injection rates. In this regime, the heavy viscoplastic fluid initially emerges from the inlet as a cylinder, creating a jet-like behavior. Depending on the injection rates, two different types of separation can be observed. When the injection velocities are moderate, the heavy fluid accumulation near the inlet leads to instabilities and separation of some injected fluid from the bulk. In contrast, at lower injection rates, the injected heavy fluid forms a cylindrical shape, which thins and separates over time. Following separation, the individual separated pieces, influenced by the interfacial shear stress applied by the surrounding fluid, gradually bend and deviate from their cylindrical shape towards a more semispherical to spherical form, as observed in relevant previous studies [40,98]. The continuous injection of heavy fluid also causes a sedimentation-like process of the fluid pieces at the end of the pipe.

4. Mixing regime

Figure 3(d) presents the image sequences depicting this particular flow regime. The mixing regime is typically observed at high inclination angles, large density differences, relatively small yield stresses, and moderate to large injection rates. In this regime, as in the other three, a buoyant jet is initially formed, with mixing occurring pipe-wide, where the average height of mixed heavy fluid over time equals the pipe diameter. A continuous viscoplastic fluid injection reveals two distinct mixing mechanisms. High injection velocities lead to a mixing region near the inlet, dominated by the heavy fluid due to inertial and buoyant force interactions. Continuous heavy fluid injection peaks its concentration in this area, followed by diffusion towards the pipe end, increasing the concentration longitudinally over time. At moderate injection rates, the heavy viscoplastic fluid uniformly spreads in the *in situ* fluid due to enhanced buoyancy from high-density differences and inclinations, and low yield stress and velocity, resulting in a gradual concentration variation and effective mixing.

Figures 4(a)–4(d) depict the spatiotemporal diagrams of the normalized depth-averaged concentration field of the heavy fluid, which corresponds to the experiments depicted in Figs. 3(a)–3(d). The colormap in the diagram depicts the mean value of the heavy fluid concentration $\overline{\overline{C}}(x,t)$, averaged across the pipe diameter at time t and position x. Note that

$$\overline{C}(x,z,t) = \int_{-\tilde{y}}^{+\tilde{y}} C(x,y,z,t)dy, \tag{6}$$

$$\overline{\overline{C}}(x,t) = \int_{0}^{1} \bar{C}(x,z,t)dz, \tag{7}$$

where $\tilde{y} = ((\frac{1}{2})^2 - y^2)^{1/2}$. Also, $C(x,y,z,t)$ represents the actual concentration field, while $\overline{C}(x,z,t)$ denotes the concentration field captured in the side-view experimental images by the camera. The diagram of Figs. 4(a)–4(d) gives some insights into the heavy fluid position, flow patterns and features, and the degree of mixing between the fluids within the flow domain.

Figure 4(a) represents the spatiotemporal diagram corresponding to the experiment shown in Figure 3(a) for the stable slumping flow regime. In this figure, the inverse slope of the black dotted line, representing the average front velocity ($\overline{V}_f$) from the beginning to the pipe end, closely aligns with the position of the heavy viscoplastic fluid front. In other words, the front velocity remains nearly constant from the start of the injection until the heavy fluid front reaches the pipe end. Likewise, when the heavy fluid hits the flow domain end and its front returns toward the injection inlet, a nearly constant backflow velocity is observed, as indicated by the solid black line superimposed on the spatiotemporal diagram. This figure shows a nearly uniform average concentration profile throughout the experiment, exept for a small mixing zone marked by solid cyan lines (when the front hits the end wall and returns). This zone may result from the interaction between the miscible heavy fluid front and the *in situ* fluid, intensified at the pipe end, or from interactions between returning and forward-moving heavy fluid in the slumping stage.

Figure 4(b) shows that this flow is unstable compared to the stable slumping regime, with more pronounced mixing. For instance, high concentrations of the heavy fluid near the inlet mark a buoyant jet and a mixing zone, with the inverse slope of the pink dash-dotted line indicating the jet average velocity ($\overline{V}_j$). In this region, thin, oblique narrow mixing layers (seen as alternating dark and light patterns) ascend against the injection direction, marked by white dash-dotted lines, whose average velocities ($\overline{V}_m$) remain nearly constant. This movement results from the closed-end flow geometry, where the injected heavy fluid's volume is counterbalanced by an equal amount of the outward-moving *in situ* Newtonian fluid or light-heavy fluid mixture. Further from the inlet, these layers either disappear or show varying velocities [55]. In fact, once a sufficiently high concentration of the heavy fluid forms, a slumping pattern appears due to the dominance of buoyancy, with a front moving at a nearly constant velocity. This is likely due to the reduced inertial stress (influenced by the nearby mixing region), which is overcome by the buoyant stress in later flow stages. In this

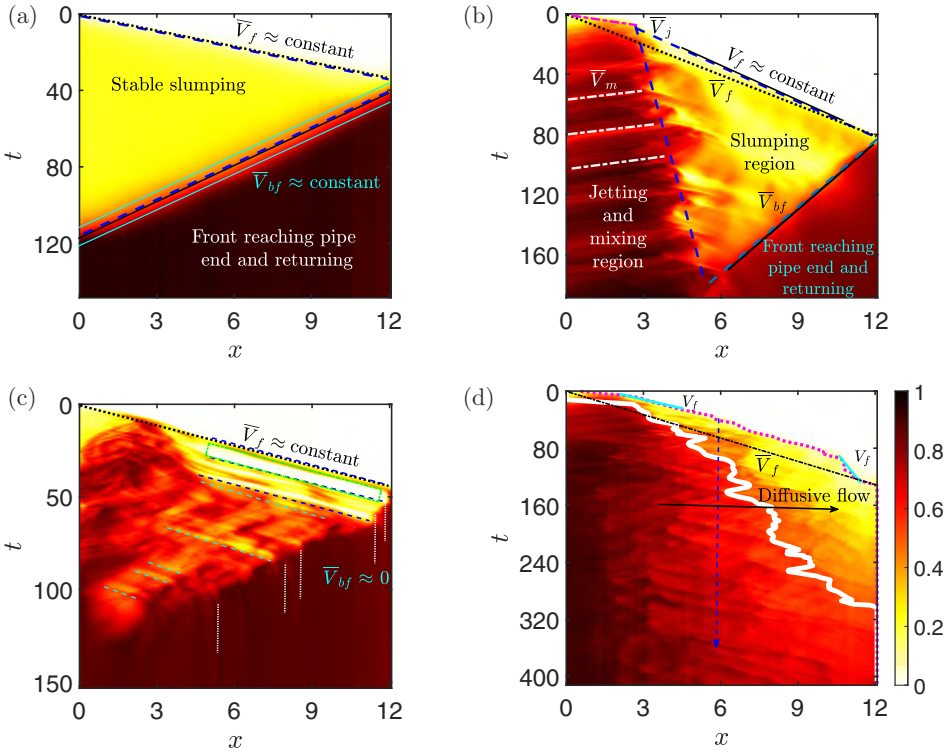

FIG. 4. Panels (a)–(d) show spatiotemporal diagrams of four regimes illustrated in Figs. 3(a)–3(d): stable slumping, unstable slumping, separation, and mixing. Panel (a) has a black dotted average front velocity line ($\overline{V}_f$), blue dashed stable slumping delimiter, solid black average backflow velocity line ($\overline{V}_{bf}$), and cyan heavy fluid mixing lines. Panel (b) includes a pink dash-dotted jet velocity line ($\overline{V}_j$), white dash-dotted returning fluid velocity lines ($\overline{V}_m$), solid black constant heavy fluid front velocity line, black dotted average flow velocity line, blue dashed flow pattern lines, and a black backflow velocity line. Panel (c) features a black dotted average flow velocity line, a blue dashed constant front velocity line, a green hollow rectangle for the separation zone, cyan dashed layer narrowing lines, and white dotted zero backflow velocity lines. Panel (d) displays an average front velocity (dash-dotted line), time-dependent position of the heavy fluid front (pink dotted line), variable front velocity (cyan solid line), a thick white line at $\overline{\overline{C}}(x,t) = 0.5$, a black arrow for diffusive flow, and a dashed arrow showing concentration increase from the injection inlet. The colorbar corresponds to the concentration of the heavy fluid in all panels.

regime, our results (omitted for brevity) also indicate that higher injection rates accelerate the mixed region formation, with negligible impact on the slumping dynamics, while larger density differences amplify interfacial instabilities due to Kelvin-Helmholtz-type instabilities.

In Figure 4(c), the white region bordered by the green dashed lines represents a separation in the heavy fluid. In fact, the white region in this spatiotemporal diagram indicates the presence of more than one front in an experiment: one represents a separated piece, and the other is either another separated piece or a region of the heavy fluid bulk. Nearly vertical lines in the returning fluid region signify zero backflow front velocity ($V_{bf} = 0$), as separated fluid pieces settle at the pipe end until more fluid accumulates. The cyan dashed lines, nearly parallel to the front velocity line, indicate narrowed layers that apply shear on the viscoplastic fluid, promoting to the formation of separated pieces.

Figure 4(d) depicts the nonuniform advancement of the heavy fluid front in the mixing regime, with the horizontal arrow indicating diffusive flow and a downward arrow signifying an increase in the concentration in the flow domain with time. The flow comprises some stages such as a buoyant

jet, development of a high-concentration heavy fluid mixing region near the inlet, a diffusive stage, and a feeding stage where the fluid mixture near the pipe end is replenished through diffusion. The thick white line marks $\overline{\overline{C}}(x,t) = 0.5$, revealing a concentration gradient generally decreasing, except near the inlet ($x < 3$), where the concentration variation remains small due to the initial heavy fluid accumulation and subsequent diffusion. In addition, there are no backflow signatures at the pipe end, suggesting that continuous mixing and diffusion enrich the concentration field there.

Note that our "diffusive flows" concern macroscopic diffusivity ($\hat{D}_M$) reflecting the random displacements of small fluid volumes, while molecular diffusivity ($\hat{D}_m$) pertains to individual molecules [99]. In fact, $\hat{D}_M$ estimated as $\hat{D}_M \sim \hat{v}\hat{\ell}$ involves a characteristic distance traveled ($\hat{\ell}$) and a characteristic velocity ($\hat{v}$) [100] and can be 10^5 times larger than $\hat{D}_m$ [53,100]. In other words, the molecular diffusivity of the fluids used is very small and, thus, it is irrelevant to the mixing processes in our experiments. Therefore, our macroscopic mixing is driven by fluid displacements, not molecular diffusion.

In our macroscopically diffusive flows and similar cases in the literature [53], efficient mixing is due to buoyancy-driven turbulence [53,59,99,100], with high injection rates also typically present. Therefore, buoyancy-driven turbulence, along with imposed inertia, causes mixing. Also, Seon *et al.* [101] identified Rayleigh-Taylor and Kelvin-Helmholtz instabilities as contributors to mixing in such flows. Thus, our diffusive flow is associated with hydrodynamic instability, secondary, and turbulent flows.

To provide a better visualization of the flow regime discussed, the online Supplemental Material [102] contains four videos corresponding to the following: the stable slumping regime with $\mathrm{Re} = 56$, $M = 0.09$, $B = 10.3$, $\beta = 15^\circ$, and $\mathrm{Fr} = 0.49$; the unstable slumping regime with $\mathrm{Re} = 1288$, $M = 0.22$, $B = 2.6$, $\beta = 15^\circ$, and $\mathrm{Fr} = 4.7$; the separation regime with $\mathrm{Re} = 418$, $B = 1.46$, $M = 0.1$, $\beta = 70^\circ$, and $\mathrm{Fr} = 3.2$; the mixing regime with $\mathrm{Re} = 1151$, $B = 0.95$, $M = 0.15$, $\beta = 86^\circ$, and $\mathrm{Fr} = 3.2$.

B. Regimes classification

To systematically differentiate the flow regimes, let us analyze concentration profiles, pseudointerface height profiles, and heavy fluid front positions, as shown, respectively, in Figs. 5(a)–5(c) for the experiments illustrated in Figs. 3 and 4. Figure 5(a) features the profiles of $\overline{\overline{C}}(x,t)$ when the heavy fluid front reaches the pipe end ($t = t_f$) for the four flow regimes. The uniform concentration profile [$\overline{\overline{C}}(x,t)$] in the stable slumping regime indicates minimal mixing. In the separation regime, the concentration profile displays zero values at certain points, signifying heavy fluid front separations. Near the pipe end, a decreasing trend in the concentration signifies the mixing regime, while the unstable slumping regime shows constant or slightly variable concentrations.

Figure 5(b) illustrates the pseudointerface height (h) at $t = t_f$ for different flow regimes. The term "pseudointerface" is used because accurately determining the interface height for two miscible fluids is challenging, particularly in the presence of instability and mixing. The red line, with h close to 1 across most of the flow domain, represents the mixing regime with strong mixing. The blue line, showing consistently decreasing (relatively small) values of h, indicates the stable slumping regime. The orange line, displaying zero values of h in certain sections, corresponds to the separation area in the separation regime. The green line, indicative of the unstable slumping regime, depicts an unstable interface.

Figure 5(c) shows that time-dependent heavy fluid front positions initially align for all regimes (when $x \lesssim 3$), but then diverge. The stable slumping is indicated by linear changes, denoting nearly constant front velocity. In contrast, the mixing regime exhibits irregular variations further from the inlet, while the separation and unstable slumping regimes display less distinct patterns.

To identify the flow regimes in an automated manner, using quantitative measures, we employ hierarchical clustering on a 3D dataset from all experiments. This dataset comprises dominant amplitude obtained from a fast Fourier transform (FFT) analysis of the concentration profiles at

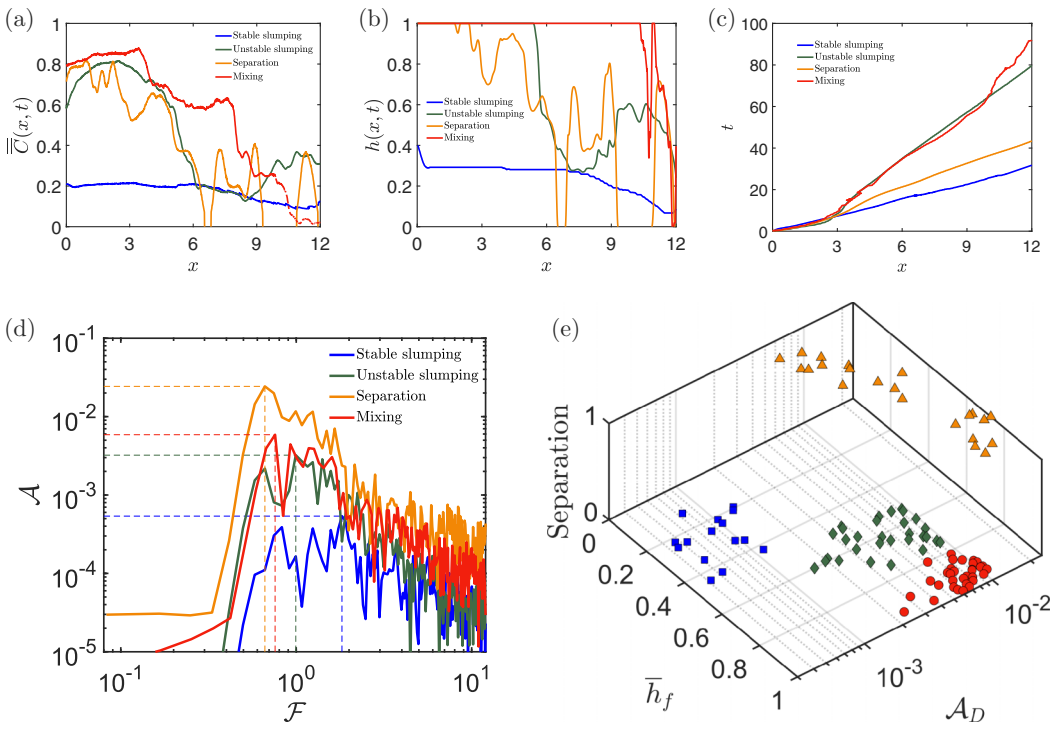

FIG. 5. (a) $\overline{\overline{C}}(x,t)$ and (b) interface heights vs x for different flow regimes at $t = t_f$ when the heavy fluid front reaches the pipe end. (c) Time-dependent positions of the heavy fluid front. (d) Dimensionless amplitude ($\mathcal{A}$) vs frequency ($\mathcal{F}$) from FFT analysis on the concentration profile, post high-order polynomial fit subtraction. In panels (a)–(d), line colors of blue, green, orange, red correspond to stable slumping, unstable slumping, separation, and mixing regimes, respectively, corresponding to Figs. 3(a)–3(d). (e) Hierarchical clustering results with four clusters on a 3D dataset, including dominant amplitude ($\mathcal{A}_D$), average interface height ($\overline{h}_f$) at $t = t_f$, and binary separation indicators. Clusters are marked for stable slumping (blue squares), unstable slumping (green diamonds), separation (orange triangles), and mixing (red circles).

$t = t_f$ (after a high-order polynomial fit subtraction), arithmetic average of h at $t = t_f$ (denoted $\overline{h}_f$) over the length of the flow domain, and binary numbers, representing by 0 or 1. In this study, a binary value of "1" is assigned to an experiment if there is a region with zero values of $\overline{\overline{C}}(x,t)$ behind the heavy viscoplastic fluid front (separation regime); otherwise, "0" is allocated (other regimes). Figure 5(d) illustrates an example of the dimensionless amplitude versus frequency from the FFT analysis, indicating that stable slumping and separation regimes have the lowest and highest dominant amplitudes ($\mathcal{A}_D$), respectively, while unstable slumping and mixing regimes exhibit similar amplitudes. Figure 5(e) shows four clusters: the cluster with the lowest $\overline{h}_f$ and $\mathcal{A}_D$ (blue squares) aligns with the stable slumping regime; moderate values of both $\overline{h}_f$ and $\mathcal{A}_D$ (green diamonds) align with the unstable slumping regime; moderate $\mathcal{A}_D$ but high $\overline{h}_f$ (red circles) correspond to the mixing regime; and high $\mathcal{A}_D$ across varying $\overline{h}_f$ values (orange triangles) are associated with the separation regime.

Figure 6(a) illustrates the flow regimes on a dimensionless plane ($\hat{V}_0$ versus $\hat{\tau}_y$) where, as seen, the data points from different regimes are not segregated. Therefore, to effectively classify these regimes, appropriate dimensionless quantities are needed for the transformation of the flow regime data into useful information. To achieve this, establishing a balance between appropriate stresses is necessary. It may be expected the longitudinal buoyant stress tends to pull the heavy fluid downward

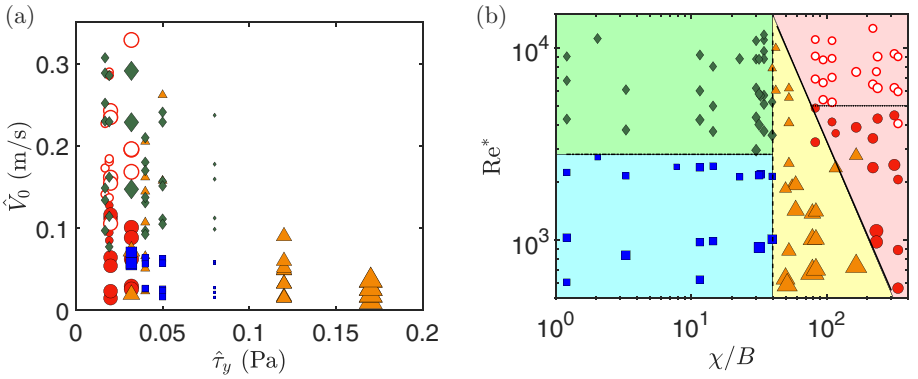

FIG. 6. Flow regimes in the dimensionless plane of $\hat{V}_0$ and $\hat{\tau}_y$ with marker size representing $\Delta\hat{\rho}$ and symbols for stable slumping (■), unstable slumping (♦), separation (▲), and mixing (○,●) regimes. (b) Flow regimes in the dimensionless plane of Re^* and χ/B with marker size representing average heavy viscoplastic fluid front velocity across the flow domain ($\overline{V}_f$). The horizontal dash-dotted line (Eq. (10)) delineates stable from unstable slumping regimes, the vertical dashed line (Eq. (11)) separates slumping from separation regimes, and the oblique solid line (Eq. (12)) marks the boundary between mixing and separation regimes. Within the mixing regime, the dotted line (Eq. (15)) marks the transition between diffusive (○) and nondiffusive (●) subregimes.

and push the light fluid upward, potentially causing interfacial instabilities and mixing. However, the yield stress aims to preserve the interface shape and structure. Thus, a balance can be struck between the characteristic longitudinal buoyant stress ($\Delta\hat{\rho}\hat{g}\hat{D}\sin\beta$) and the yield stress ($\hat{\tau}_y$) as

$$\Delta\hat{\rho}\hat{g}\hat{D}\sin\beta \sim \hat{\tau}_y \quad \Rightarrow \quad \frac{\Delta\hat{\rho}\hat{g}\hat{D}\sin\beta}{\hat{\tau}_y} \propto \frac{\mathrm{Re}\sin(\beta)}{\mathrm{Fr}^2 B} = \frac{\chi}{B}. \tag{8}$$

However, our experiments indicate that increasing the injection velocity generally leads to a move from stable to unstable flows. This can be expressed by balancing the characteristic inertial stress ($\frac{1}{2}(\hat{\rho}_H + \hat{\rho}_L)\hat{V}_0^2$) and the characteristic viscous stress of the *in situ* fluid ($\hat{\mu}_L \frac{\hat{V}_0}{\hat{D}}$):

$$\hat{\mu}_L \frac{\hat{V}_0}{\hat{D}} \sim \frac{1}{2}(\hat{\rho}_H + \hat{\rho}_L)\hat{V}_0^2 \quad \Rightarrow \quad \frac{(\hat{\rho}_H + \hat{\rho}_L)\hat{V}_0\hat{D}}{2\hat{\mu}_L} = \frac{\mathrm{Re}}{M} = \mathrm{Re}^*, \tag{9}$$

where $\mathrm{Re}^* = \frac{\mathrm{Re}}{M}$ is modified Reynolds number.

Based on the dimensionless groups found above, Figure 6(b) illustrates the regime classification map in the plane of χ/B and Re^*. The data points are reasonably segregated. The stable slumping regime features low Re^* and χ/B, while high Re^* and low χ/B mark the unstable slumping regime. The separation and mixing regimes occur at the highest χ/B values, with the mixing usually occurring when χ/B is relatively larger as well. Accordingly, the crude transition boundaries can be established as

$$\text{Stable-unstable slumping transition: } \mathrm{Re}^* \approx 2800, \tag{10}$$

$$\text{Slumping-separation transition: } \frac{\chi}{B} \approx 40, \tag{11}$$

$$\text{Separation-mixing transition: } \mathrm{Re}^* \approx -50\frac{\chi}{B} + 15\,000. \tag{12}$$

These transition boundaries indicate that at low χ/B, increasing the injection rate shifts the flow from the stable to unstable slumping regime, and at high χ/B, it transitions the flow from the separation to mixing regime. Also, increasing the density difference leads to a transition from the

slumping to separation, then to mixing regime. Moreover, a higher yield stress moves the flow from the mixing to separation, and ultimately to slumping regime.

Before proceeding, let us briefly comment on the effects of geometrical parameters on flow characteristics and regimes. Note that, in this study, parameters, such as the aspect ratio and eccentricity, are fixed due to experimental limitations. However, their general effects may be inferred from previous research. Akbari and Taghavi [22] explored the impact of the aspect ratio by varying flow domain length ($\hat{L}$) in buoyant miscible high-yield stress fluid injections, finding that reducing $\hat{L}$ causes the heavy fluid front to reach the pipe end before slumping begins, decreasing mixing and favoring stable flows [13]. Also, Akbari and Taghavi [22] and Ghazal and Karimfazli [92] showed that eccentricity has less impact on flow regime transitions for similar type flow. Akbari and Taghavi [22] further found that variations in the diameter ratio affect regime transition boundaries nonmonotonically, with similar findings by Ghazal and Karimfazli [92] regarding concentration fields. Based on these studies, we expect our flow regimes and transitions to be more affected by pipe length (and aspect ratio), with secondary flow patterns such as slumping, diffusive, and separation not occurring in shorter flow domains. In contrast, eccentricity may be expected to have a lesser impact on our flow regimes and characteristics.

Mixing subregimes

Experiments in the mixing regime reveal two distinct patterns: diffusive and nondiffusive subregimes. The diffusive mixing involves efficient mixing of the heavy viscoplastic fluid with the lighter Newtonian fluid, characterized by spreading from high to low concentration areas. In contrast, the nondiffusive mixing usually occurs during the bulk movement of the heavy fluid. Our experimental data indicates that the diffusive mixing is slower compared to the nondiffusive mixing. Also, the nondiffusive mixing results in more uniform concentration profiles across the pipe domain than the diffusive mixing. Typically, the diffusive mixing occurs at higher injection velocities, while the nondiffusive mixing is observed at lower injection rates.

Diffusive flow patterns have been studied, traditionally for Newtonian flows, e.g., in exchange flows in vertical [99,100] and inclined pipes [101,103,104], as well as displacement flows in inclined [53,59] and moving pipes [105]. For such flows, Debacq *et al.* [99,100] highlighted the dominance of macroscopic diffusivity over molecular diffusivity in governing flow characteristics and, along with Seon *et al.* [101], used a similarity scaling ($\frac{\hat{x}}{\sqrt{\hat{t}}}$) to analyze depth-averaged concentration profiles. Alba *et al.* [53] and Amiri *et al.* [105] extended the similarity scaling to $\frac{\hat{x}-\hat{V}_0\hat{t}}{\sqrt{\hat{t}}}$ for injection and displacement flows, assuming a uniform imposed velocity ($\hat{V}_0$). However, our analysis found the proposed similarity scaling ($\frac{\hat{x}-\hat{V}_0\hat{t}}{\sqrt{\hat{t}}}$) to be ineffective in assessing macroscopic diffusivity, particularly due to our unique flow configuration, with adjacent inlet and outlet boundaries and closed-end geometry. In fact, the typical assumption of a mixture core moving at $\hat{V}_0$ is incompatible with our work, particularly due to unique stages in our viscoplastic fluid injection. To accommodate these flow stages, we propose a new similarity scaling in dimensionless form as

$$\xi = \frac{(x - \overline{V}_f t/2)}{\sqrt{t}}, \tag{13}$$

where $\overline{V}_f$ is the average front velocity, leading to the following similarity solution for the depth-average concentration evolution profiles:

$$\overline{\overline{C}}(x,t) \equiv \overline{\overline{C}}(\xi) = \frac{1}{2}\mathrm{erfc}\left(\frac{\xi}{2\sqrt{D_M}}\right). \tag{14}$$

Here, D_M is the dimensionless macroscopic diffusivity, which is defined as $D_M = \frac{\hat{D}_M}{\hat{V}_0\hat{D}}$, where $\hat{D}_M$ is the dimensional macroscopic diffusivity.

Applying Eq. (14) to our experimental depth-averaged concentration profiles allows us to determine whether our mixing flows are diffusive or nondiffusive. Figure 7 shows two examples:

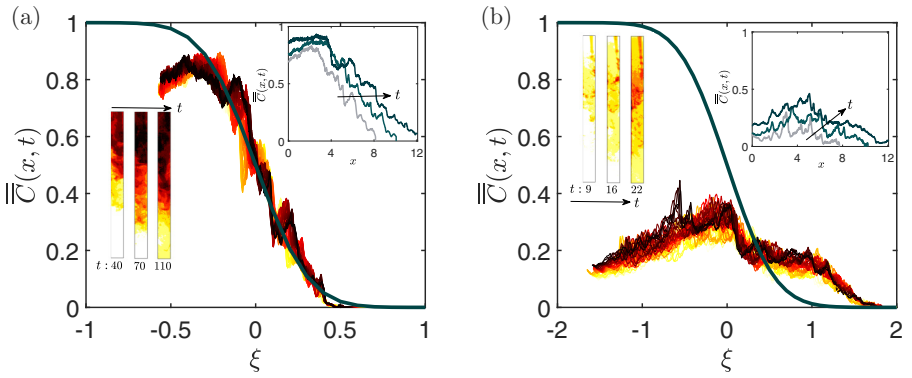

FIG. 7. Convergence of depth-averaged concentration profiles $[\overline{\overline{C}}(x,t)]$ vs $\xi = (x - \overline{V}_f t/2)/\sqrt{t}$ for an experiment with (a) Re = 701, Fr = 2.67, $M = 0.12$, $B = 0.58$, and $\beta = 90^\circ$ and (b) Re = 242, Fr = 1.11, $M = 0.1$, $B = 1.17$, and $\beta = 70^\circ$. In both panels, insets illustrate experimental snapshots and $\overline{\overline{C}}(x,t)$ vs t. In panel (a), the solid dark-green line represents the fitting of the error function, Eq. (14), using $D_M = 0.035$.

in Figure 7(a), the concentration profiles align reasonably onto a single curve corresponding to Eq. (14), indicating a diffusive flow, while in Figure 7(b), despite the collapsed profiles, they do not fit Eq. (14), suggesting a nondiffusive flow. Accordingly, the mixing regime experiments in Figure 6 are classified as diffusive (hollow) or nondiffusive (filled) subregimes, based on whether Eq. (14) aligns their profiles onto a master curve, with the onset around:

$$\text{Transition between diffusive and nondiffusive mixing subregimes: } \mathrm{Re}^* \approx 5000. \tag{15}$$

Figure 6 shows that diffusive flows are prevalent at high χ/B and Re^*, indicating they occur under high buoyant and inertial stresses, and low yield and viscous stresses.

Focusing on the diffusive flow subregime experiments, dimensional and dimensionless macroscopic diffusion coefficients range from 1.3×10^{-5} to 2×10^{-4} (m^2/s) and 0.01 to 0.044, respectively, aligning with the ranges previously reported [53,59,100,105]. Our results (omitted for brevity) also reveal that higher density differences increase macroscopic diffusivity, enhancing diffusion from higher to lower heavy fluid concentrations. However, the injection velocity has no clear impact on macroscopic diffusivity but primarily forms a high-concentration mixing region near the inlet, initiating diffusion which subsequently becomes less dependent on injection velocity. In dimensionless forms, higher χ/B values are associated with increased dimensionless macroscopic diffusivity, indicating that rising buoyant stress enhances diffusivity, whereas changes in Re^* have no effect on it.

C. Interfacial velocities

This section analyzes interfacial velocities in our viscoplastic injection flows, focusing specifically on the heavy fluid front velocity, separated piece falling velocity, and backflow front velocity.

1. Front velocity

This section quantifies the front velocity ($\hat{\overline{V}}_f$) of the heavy fluid, as a crucial measure of the flow dynamics, calculated as the average front velocity across the flow domain, for the inlet until the fluid front reaches the pipe end. Figure 8(a) shows the experimental average front velocity ($\hat{\overline{V}}_f$) versus the mean injection velocity $\hat{V}_0$, with the marker color and size representing $\hat{\mu}_H$ and β values, respectively. The data points scatter in this dimensional plane without a clear trend, indicating the need for a detailed analysis in dimensionless form for a better understanding.

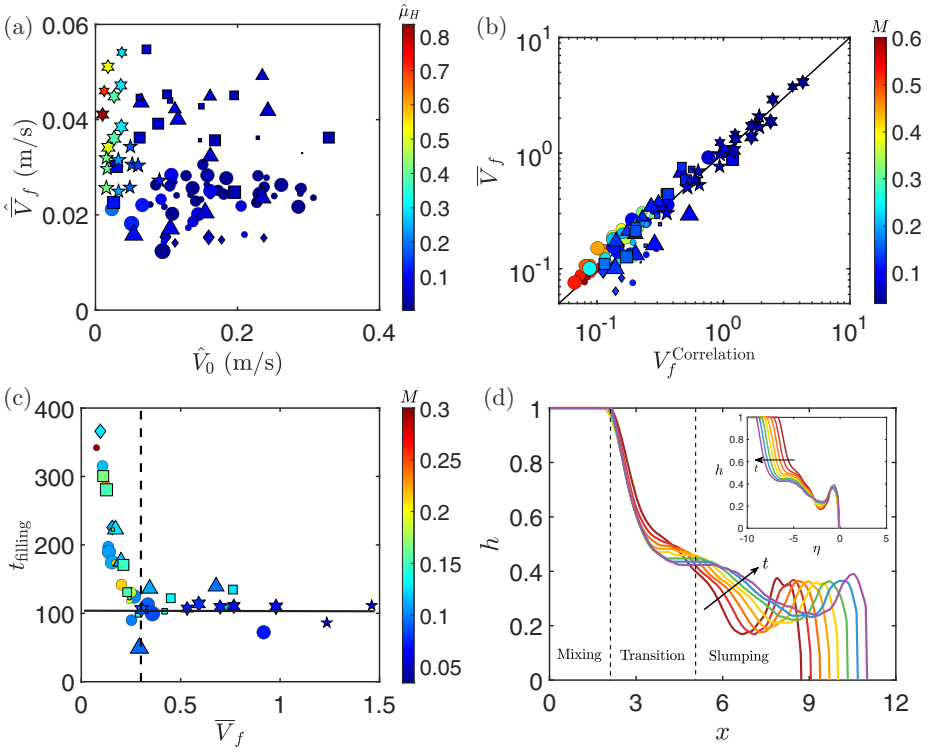

FIG. 8. (a) $\hat{\overline{V}}_f$ versus $\hat{V}_0$, with marker colors and sizes representing $\hat{\mu}_H$ and β. (b) Experimental $\overline{V}_f$ versus $V_f^{\text{Correlation}}$ (Eq. (17)), and the 1:1 line shown as the solid line. (c) t_{filling} versus $\overline{V}_f$, with the vertical line at $\overline{V}_f = 0.3$ and the horizontal line at $t_{\text{filling}} \approx 100$. In panels (b) and (c), marker colors and sizes denote M and β. Symbols represent $\Delta\hat{\rho}$: hexagrams [38 (kg/m^3)], squares [20 (kg/m^3)], triangles [18 (kg/m^3)], pentagrams [17 kg/m^3)], circles [6 (kg/m^3)], and diamonds [1 (kg/m^3)]. (d) Time-dependent pseudointerface height change over $t = [80 : 5 : 120]$ (arrow direction) for an unstable slumping regime experiment, with Re = 890, $M = 0.13$, Fr = 13, $B = 2.26$, and $\beta = 15^\circ$. The inset x axis uses $\eta = x - V_f t$ as a moving frame of reference, to collapse frontal pseudointerface height profiles.

Previous studies [55,56,106] have shown that buoyancy strength relative to inertia predominantly influences the front velocity in similar flows, leading to its proportionality with the characteristic buoyant-inertial velocity $\sqrt{At\hat{g}\hat{D}}$, derived from balancing buoyancy and inertial stresses. Thus, one can write

$$\hat{V}_f \propto \sqrt{At\hat{g}\hat{D}} \quad \Rightarrow \quad V_f = \frac{\hat{V}_f}{\hat{V}_0} \propto \frac{\sqrt{At\hat{g}\hat{D}}}{\hat{V}_0} = \frac{1}{\text{Fr}}. \tag{16}$$

However, we may expect the front dynamics and, thus, the front velocity to be moderately influenced by M, B and β, and, to crudely incorporate these effects, we propose an expansion for the average front velocity:

$$V_f \approx \frac{a_1}{\text{Fr}} + \log(M)[a_2 + a_3 B + a_4 \sin(\beta)], \tag{17}$$

which reverts to $V_f \approx \frac{a_1}{\text{Fr}}$ as $M \to 1$ (i.e. the isoviscous case). The unknown constant coefficients of Eq. (17) (i.e., a_i with $i = 1, 2, 3, 4$), are determined through curve fitting using the experimental

data, resulting in

$$V_f \approx \frac{0.47}{\mathrm{Fr}} + \log(M)[-0.066 - 0.0035B + 0.056\sin(\beta)]. \tag{18}$$

Figure 8(b) shows the front velocities calculated by Eq. (18) against the average front velocity experimental data ($\overline{V}_f$), demonstrating a reasonable match, with a coefficient of determination at 0.97 and a root-mean-square error of 0.12.

Considering the front velocity proves to be useful for understanding other characteristics of the flow. For instance, from a practical viewpoint, we define the filling time (t_{filling}) as the duration for the injection fluid to occupy the flow domain. Figure 8(c) shows t_{filling} against $\overline{V}_f$, with symbol sizes and colors indicating β and M. The results reveal a rapid initial decrease in t_{filling}, aligning with Eq. (18) that associates decreasing t_{filling} with lower Fr (higher buoyant stresses or density differences); this is consistent with prior research [55,106]. However, once $\overline{V}_f \gtrsim 0.3$, a further increase in $\overline{V}_f$ does not correspond to a significant decrease in t_{filling}. Based on Eq. (18), this critical condition (i.e., $\overline{V}_f = 0.3$) corresponds to

$$\mathrm{Fr}^{\text{critical}} \approx \frac{0.47}{0.3 - \log(M)[-0.066 - 0.0035B + 0.056\sin(\beta)]}. \tag{19}$$

Beyond this critical point, variations in the flow parameters do not significantly reduce t_{filling}, which stabilizes around $t_{\text{filling}} \approx 100$. This indicates that, for example, increasing the density difference to enhance $\overline{V}_f$ and reduce t_{filling} is effective only up to a certain limit. Past this point, dominant Rayleigh-Taylor instabilities due to large density differences, and increased Kelvin-Helmholtz instabilities at higher front velocities, counteracting the longitudinal buoyancy as driving force, lead to a nearly constant t_{filling}.

The front velocity analysis also aids in understanding frontal dynamics through analyzing pseudointerface height profiles. Figure 8(d) shows a typical pseudointerface height evolution in the unstable slumping regime, with segments including the mixing region near the inlet, transition to the slumping region, and the slumping region itself. The inset, using the moving frame of reference $\eta = x - V_f t$, shows pseudointerface height profiles converging to a self-similar curve at the front (resembling a steady-traveling wave), but not in the mixing and transition regions.

2. Separated piece velocity

In the separation regime, a repetitive detachment and, subsequently, falling of viscoplastic fluid pieces (i.e., separated from the bulk injected fluid) occurs when, among other factors, the longitudinal buoyant stress overcomes the yield stress. Once detached, the separated pieces undergo quick deformation into a quasi-spherical shape, due to forces such as drag; this aligns with previous findings involving separations in viscoplastic [83] and highly viscous [56] displacements. Similar behaviors are also observed in satellite drop formations in various flow configurations across multiple studies [28–30,37,40,107–113].

In our experiments, as the separated pieces surrounded by the *in situ* fluid settle towards the pipe end, they experience significant drag force while falling due to gravity. To understand the dynamics of these settling pieces, we propose a very crude balance between the longitudinal buoyancy and drag forces for a falling piece:

$$\frac{4}{3}\pi\left(\frac{\hat{D}}{2}\right)^3 \times \Delta\hat{\rho}\hat{g}\sin(\beta) = 4\pi\left(\frac{\hat{D}}{2}\right)^2 \times \frac{1}{2}\hat{\rho}_L C_d \hat{V}_s^2, \tag{20}$$

in which C_d denotes the drag coefficient. Equation (20) presupposes that the flow is steady, the yield stress roughly preserves the falling piece shape (i.e., avoiding mixing), and the falling piece is quasi-spherical, with an equivalent diameter which is roughly of the pipe diameter. Neglecting the

wall presence and effect, the drag coefficient can be crudely estimated by [114]

$$C_d = \frac{24}{\mathrm{Re}_s}\left[1 + [8.1716\exp(-4.0655\phi)]\mathrm{Re}_s^{(0.0964+0.05565\phi)}\right] + \frac{73.69\mathrm{Re}_s\exp(-5.0748\phi)}{\mathrm{Re}_s + 5.378\exp(6.2122\phi)}, \quad (21)$$

in which ϕ is the sphericity and Re_s is the Reynolds number of the separated piece, defined as

$$\mathrm{Re}_s = \frac{\hat{\rho}_L \hat{V}_s \hat{D}}{\hat{\mu}_L}. \quad (22)$$

Considering that our experiments show that $700 \lesssim \mathrm{Re}_s \lesssim 2700$, we write a series expansion of Eq. (21) versus the small parameter $\frac{1}{\mathrm{Re}_s}$ and, subsequently, substitute the resulting equation in Eq. (20), which after some simplifications and algebra and solving for $\hat{V}_s$ eventually leads to

$$V_s \approx \frac{2.7\exp(6.2\phi)}{\mathrm{Re}^*} + \left(\frac{7.2\exp(12.4\phi)}{\mathrm{Re}^{*2}} + \frac{\exp(5.1\phi)}{111}\frac{\sin(\beta)}{\mathrm{Fr}^2}\right)^{1/2}. \quad (23)$$

Equation (23) indicates that V_s is a function of Fr, Re^*, β, and ϕ.

To calculate ϕ, several sphericity definitions based on projected areas have been proposed in the literature [115–117], with five commonly used methods: area sphericity (ϕ_A), diameter sphericity (ϕ_D), circle ratio sphericity (ϕ_C), perimeter sphericity (ϕ_P), and width-to-length ratio sphericity (ϕ_{WL}), which are, respectively, defined as

$$\phi_{\mathrm{A}} = \frac{\hat{A}_s}{\hat{A}_{\mathrm{cir}}}, \quad \phi_{\mathrm{D}} = \frac{\hat{D}_c}{\hat{D}_{\mathrm{cir}}}, \quad \phi_{\mathrm{C}} = \frac{\hat{D}_{\mathrm{ins}}}{\hat{D}_{\mathrm{cir}}}, \quad \phi_{\mathrm{P}} = \frac{\hat{P}_c}{\hat{P}_s}, \quad \phi_{\mathrm{WL}} = \frac{\hat{d}_2}{\hat{d}_1}, \quad (24)$$

where $\hat{A}_s$ is the object's projected area, $\hat{A}_{\mathrm{cir}}$ is the area of the smallest encompassing circle, $\hat{D}_c$ and $\hat{D}_{\mathrm{cir}}$ are diameters of a circle equal to the maximum projected area and the smallest encompassing circle, respectively. Also, $\hat{D}_{\mathrm{ins}}$ is the diameter of the largest inscribing circle, $\hat{P}c$ and $\hat{P}_s$ are perimeters of a circle with the same area as the object and the object's perimeter. Finally $\hat{d}_2$ and $\hat{d}_1$ represent the object's width and length. In particular, Zheng and Hryciw [117] found that the width-to-length ratio sphericity aligns with Krumbein and Sloss's classical roundness-sphericity chart [118].

In our study, we adopt the numerical methodologies of Ref. [117] to estimate the sphericity of separated or falling pieces, using computational geometry. As an example of our results, Figure 9(a) shows the time variation of the average sphericity [arithmetic average of the five methods in Eq. (24)] for a falling piece, with the dashed lines indicating an average sphericity ($\phi = 3/4$) from separation to settling. Consequently, we assume an average sphericity of $\phi \approx 3/4$ for the first separated pieces in this study.

Figure 9(b) shows the experimental average velocities of the first falling separated piece ($\overline{V_s}$) compared to Eq. (23) results, demonstrating reasonable agreement. The data also suggest that lower Fr values correlate with higher $\overline{V_s}$ and higher Re^* values correspond to smaller $\overline{V_s}$, both in line with Eq. (23).

Despite many simplifications in Eq. (23), it compares well with the experimental results, albeit with differences arising from various factors. For example, Eq. (23) overlooks deformation of separated pieces, and deviations may be due to limited falling heights, irregular piece shapes, density variations between separated heavy fluid pieces and *in situ* fluid, and interactions with pipe walls, leading to discrepancies between $\overline{V_s}$ and Eq. (23) results.

3. Backflow front velocity

The backflow interfacial velocity appears, as discussed in Section III A, when the heavy fluid front reaches the pipe end and returns backward. This feature is particularly significant in the unstable slumping regime (typically with $\beta \lesssim 45^o$), which will be the focus of this section. Understanding this velocity is crucial for evaluating the *in situ* fluid removal in the unstable slumping regime's final flow stage.

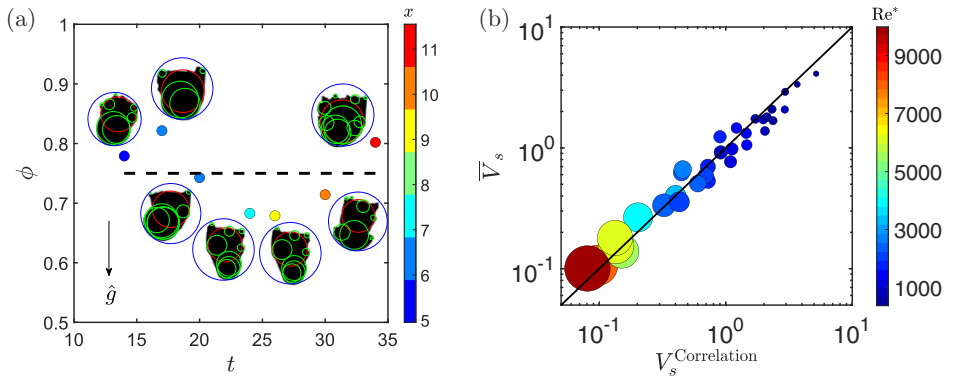

FIG. 9. (a) Time-dependent average sphericity of the first separated piece in an experiment with Re = 315, $B = 4.6$, $M = 0.09$, $\beta = 86^\circ$, and Fr = 1.6. This sphericity, calculated using Ref. [117]'s method and averaging according to Eq. (24), includes red circles showing the largest circle within the separated pieces, green circles estimating roundness (referencing Ref. [118]), and blue circles for the diameter of the smallest encompassing circle. (b) Experimental $\overline{V}_s$ versus $V_s^{\text{Correlation}}$ (Eq. (23)), with the 1:1 solid line, and the marker color and size representing Re* and Fr values, respectively.

Figure 10(a) presents the average experimental backflow velocity (i.e., $\hat{\overline{V}}_{bf}$, dimensional) versus the mean injection velocity $\hat{V}_0$, indicating a scattered distribution. This implies that, to discern more robust trends, appropriate dimensionless groups are necessary. The dynamics of heavy fluid backflow can be understood by balancing the characteristic longitudinal buoyant stress with the inertial stress resulting from the backflow front's motion:

$$\Delta\hat{\rho}\hat{g}\hat{D}\sin(\beta) \sim \tfrac{1}{2}(\hat{\rho}_H + \hat{\rho}_L)\hat{V}_{bf}^2, \tag{25}$$

leading to

$$V_{bf} \approx c\frac{\sqrt{\sin(\beta)}}{\text{Fr}}, \tag{26}$$

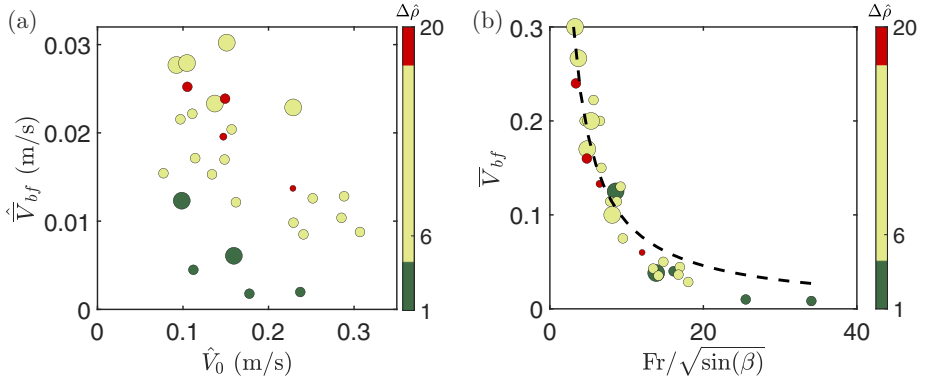

FIG. 10. (a) Experimental $\hat{\overline{V}}_{bf}$ versus $\hat{V}_0$, with marker colors indicating $\Delta\hat{\rho}$ ($\frac{\text{kg}}{\text{m}^3}$) values, and symbol sizes representing different β. (b) Experimental $\overline{V}_{bf}$ against $\frac{\text{Fr}}{\sqrt{\sin(\beta)}}$, with marker colors showing $\Delta\hat{\rho}$ ($\frac{\text{kg}}{\text{m}^3}$) values, symbol sizes representing different β, and dashed line marking Eq. (26).

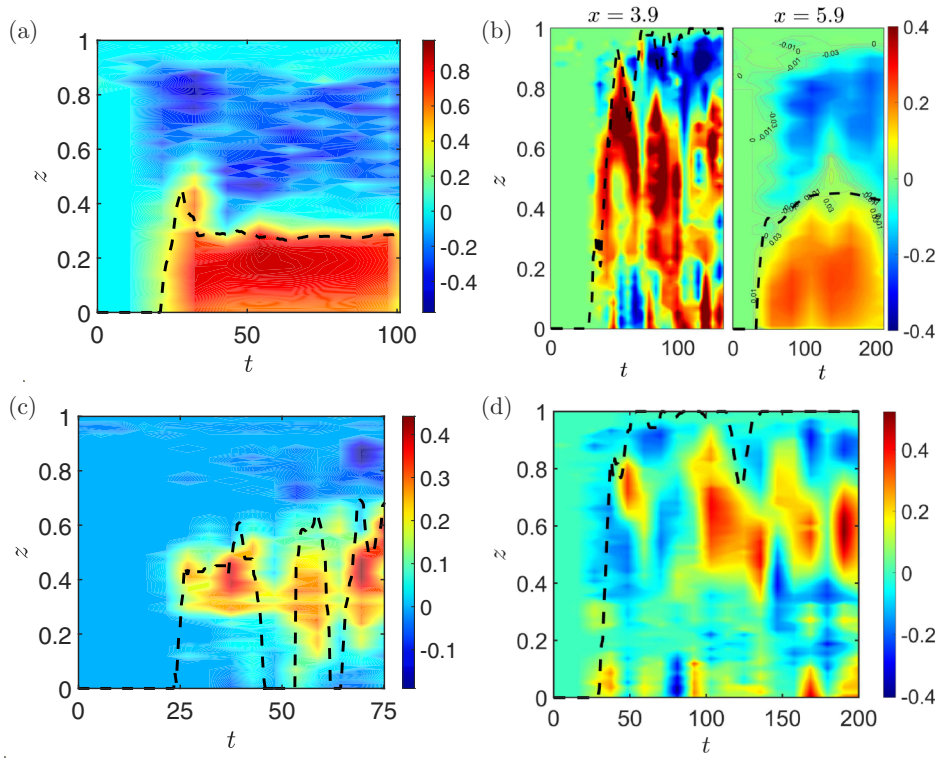

FIG. 11. Axial velocity contours from UDV measurements in the z and t plane. (a) Stable slumping regime at $x = 2$ with Re $= 193$, $B = 2.4$, $M = 0.09$, $\beta = 45°$, and Fr $= 1.7$. (b) Unstable slumping regime with Re $=$ 1270, $B = 1.19$, $M = 0.14$, $\beta = 15°$, and Fr $= 17.3$: at $x = 3.9$ (mixing stage) and at $x = 5.9$ (slumping stage). (c) Separation regime at $x = 5.3$, with Re $= 418$, $B = 1.46$, $M = 0.1$, $\beta = 70°$, and Fr $= 3.2$. (d) Mixing regime at $x = 4.9$, with Re $= 1150$, $B = 0.95$, $M = 0.15$, $\beta = 86°$, and Fr $= 3.2$. Black dashed lines in panels (a), (b) at $x = 5.9$, and (c) represent the pseudointerface height at the UDV probe location, while in panels (b) at $x = 3.9$ and (d) they represent the height corresponding to $\overline{C}(x, z, t) = 0.5$.

in which c is a constant, which can be obtained via curve-fitting to the experimental data, yielding $c = 0.92$, with a coefficient of determination at 0.9 and a root-mean-square error of 0.03.

Figure 10(b) exhibits the relationship between experimental average backflow velocity in dimensionless form ($\overline{V}_{bf}$) and $\frac{\text{Fr}}{\sqrt{\sin(\beta)}}$, aligning with the findings of Eq. (26). Higher Fr correlates with lower $\overline{V}_{bf}$, and an increase in β leads to a rise in $\overline{V}_{bf}$. However, at larger $\frac{\text{Fr}}{\sqrt{\sin(\beta)}}$, deviations occur with $\overline{V}_{bf}$ being smaller than expected by Eq. (26), particularly at lower β values. At such inclinations, as buoyant stresses are reduced, viscous stresses that Eq. (26) ignores can become significant, resulting in lower $\overline{V}_{bf}$.

D. Velocity field

Our study has so far revealed various interfacial behaviors across different flow regimes, which can be linked to their respective fluid velocity fields. Thus, to better understand the flow nature, in this section, we analyze the fluid velocity using the UDV technique results.

Figure 11(a) shows the stable slumping regime, including the experimental UDV contours of the axial velocity in the t and z plane. Here, $z = 0$ and $z = 1$ represent lower and upper pipe walls, respectively. The superimposed black dotted lines illustrate pseudointerface height through time at the UDV location. Positive velocities align with the injection direction, and negative values

correspond to the opposite direction. In this regime, the UDV results exhibit a smooth distribution of positive velocities near the lower pipe wall with negative values towards the upper wall, representing the stable slumping of the viscoplastic fluid beneath the *in situ* one.

Figure 11(b) examines the unstable slumping regime, showing the experimental UDV contours of the axial velocity in the t and z plane. The left panel of Figure 11(b) at $x = 3.9$ (near the inlet, mixing stage) shows fluctuating velocities indicating mixing, while the right panel of Figure 11(b) at $x = 5.9$ (further from the inlet, slumping stage) displays positive velocities in the lower pipe half (advancing heavy fluid) and negative in the upper half (countercurrent light fluid). The velocities are higher in the mixing stage than the slumping stage, due to the injection dynamics dominating the former, and buoyancy the latter. The superimposed black dotted lines corresponds to $\overline{C}(x, z, t) = 0.5$ and the pseudointerface height in the left and right panels of Figure 11(b), respectively, tracing the flow evolution and the heavy fluid occupation of the flow domain. In the right panel of Figure 11(b), regions with near-zero velocities (± 0.03) highlight where the pseudointerface height may roughly align with zero fluid velocity, particularly in the slumping stage.

Figure 11(c) focuses on the separation regime, presenting experimental UDV contours of axial velocity in the t and z plane, with the UDV positioned near the separation point. The figure also overlays pseudointerface height on axial velocity profiles, showing oscillations in the axial velocity at the separation points (where the pseudointerface height reaches zero) and negative velocities indicating countercurrent *in situ* Newtonian fluid flow.

Figure 11(d) addresses the mixing regime, displaying the axial velocity contours with positive and negative values in the t and z plane, reflecting the flows in both injection and opposite directions (indicative of significant mixing). In addition, the black dashed line corresponds to $\overline{C}(x, z, t) = 0.5$, demonstrating the rapid "interface" evolution in this regime.

E. Mixing index

Motivated by practical implications, let us analyze the quality of the heavy fluid placement in our injection flow process, which is tied to the mixing of the injected heavy fluid with *in situ* light fluid. We investigate this by proposing a dynamic mixing index (MI) based on concentration profiles, calculated over time:

$$\mathrm{MI}(t) = \frac{1}{A} \int_A \overline{C}(x, z, t)\, dA, \tag{27}$$

where A represents the projected area in the $x - z$ plane contaminated by the heavy fluid, defined using a numerical cutoff threshold of $\overline{C}(x, z, t) = 0.05$. Note that Eq. (27) differs from Eq. (7) as the latter provides an average concentration for each x, yielding a data set, while Eq. (27) offers a single average value for the entire contaminated flow domain. Specifically, Eq. (27) calculates average concentration profiles over the $x - z$ plane contaminated by the heavy fluid, whereas Eq. (7) determines the average concentration profiles in each x, averaged across z and y, regardless of the heavy fluid presence.

Figures 12(a) and 12(b) presents MI versus time for three different experiments in the mixing regime, analyzing the effects of Re^* (Figure 12(a)) and χ/B (Figure 12(b)). Both panels show four mixing index evolution stages: initial decrease, increase, subsequent decrease, and stabilization. In Figure 12(a), with constant χ/B and varying Re^* (increasing in the arrow direction), higher Re^* initially indicates lower MI (better fluid placement), but this reverses later, with higher Re^* resulting in larger MI (worst placement quality). In Figure 12(b), with constant Re^* and varying χ/B (increasing in the arrow direction), initially, the MI values are similar across the experiments. However, increasing χ/B consistently leads to larger MI at longer times, which is a trend dominant for most of the experimental duration.

To compare the MI values across all regimes and experiments, we define the mixing index at the time the heavy fluid front reaches the pipe end as $\mathrm{MI}_f = \mathrm{MI}(t = t_f)$. Figure 12(c) shows MI_f versus $\hat{V}_0$, displaying scattering without a clear trend. To quantify MI_f, we consider the long-term balance

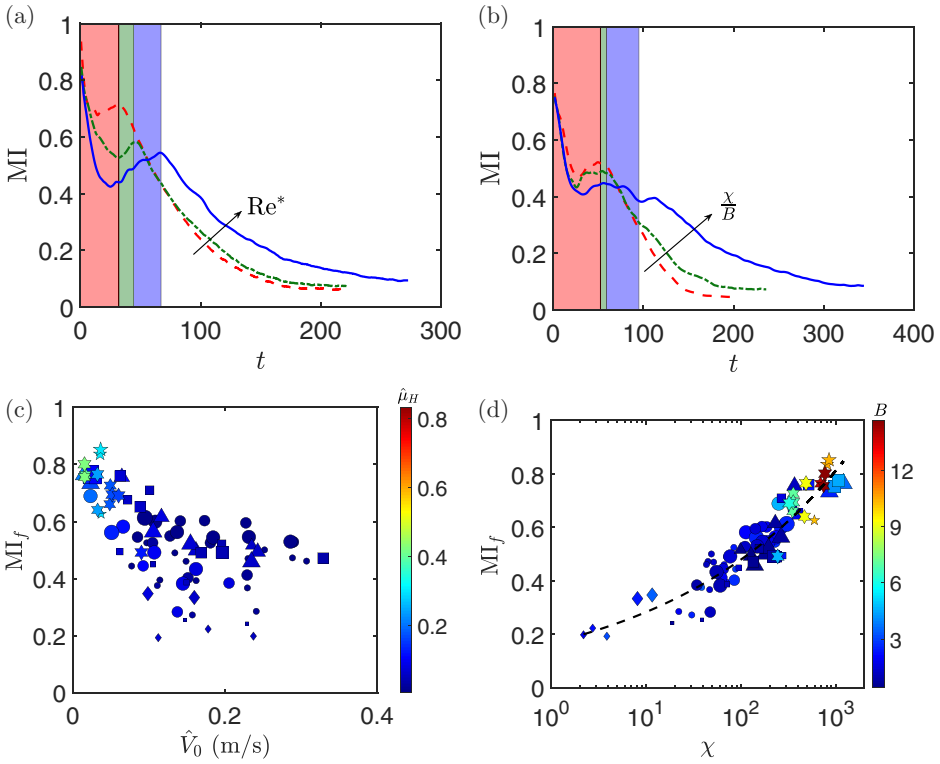

FIG. 12. (a), (b) MI plotted against t: (a) At $\frac{\chi}{B} \approx 238$, with a red dashed line for $\mathrm{Re}^* = 4292$, green dot-dash for $\mathrm{Re}^* = 6189$, and blue solid line for $\mathrm{Re}^* = 9011$, showing increasing Re^* (arrow direction). Shaded regions represent the time until the heavy fluid front reaches the pipe end, with colors matching the curves. (b) At $\mathrm{Re}^* \approx 7200$, with a red dashed line for $\frac{\chi}{B} = 165$, green dot-dash for $\frac{\chi}{B} = 220$, and blue solid line for $\frac{\chi}{B} = 233$, indicating increasing $\frac{\chi}{B}$ (arrow direction). (c) MI_f versus $\hat{V}_0$, with varying symbol sizes for different β and symbols denoting $\Delta\hat{\rho}$: hexagrams [38 (kg/m^3)], squares [20 (kg/m^3)], triangles [18 (kg/m^3)], pentagrams [17 (kg/m^3)], circles [6 (kg/m^3)], diamonds [1 (kg/m^3)]. (d) MI_f against χ, with a dashed line showing Eq. (28) results.

between the characteristic longitudinal buoyant ($\Delta\hat{\rho}\hat{g}\hat{D}\sin\beta$) and the viscous stresses ($\frac{\sqrt{\hat{\mu}_L\hat{\mu}_H}\hat{V}_0}{\hat{D}}$), leading to χ, as the main dimensionless number. As Figure 12(d) illustrates, the data points very roughly align along a fitted curve:

$$\mathrm{MI}_f \approx 0.17\chi^{0.23}, \tag{28}$$

with a coefficient of determination of 0.86 and a root-mean-square error of 0.06. Figure 12(d) shows the relationship between MI_f and χ, with the marker sizes representing β. The results reveal that a rise in χ, for instance through an increased density difference, leads to a higher MI_f. This increase in buoyancy amplifies instability, particularly Rayleigh-Taylor and Kelvin-Helmholtz instabilities, consequently elevating the mixing index. Note that this conclusion is valid for $\mathrm{At} \ll 1$. For larger At up to close to unity, previous works such as the simulation study of Huang *et al.* [119] on a wide range of density ratios have shown that less mixing occurs in a two-phase flow system as At increases toward one.

IV. SUMMARY

In this study, motivated by industrial process applications in the P&A operations of oil and gas wells, we conduct an experimental investigation on the buoyant miscible injection of heavy viscoplastic fluids (with moderate yield stresses) into a light Newtonian fluid. Our dimensional analysis and several simplifications and assumptions suggest that the flow behaviors in our experiments can be, in general, elucidated using five dimensionless numbers, namely Reynolds number (Re), Froude number (Fr), inclination angle (β), Bingham number (B), and viscosity ratio (M). Furthermore, we find that specific combinations of these numbers, such as a buoyancy number [$\chi = \frac{2\mathrm{Re}}{\mathrm{Fr}^2}\sin(\beta)$] and a modified Reynolds number ($\mathrm{Re}^* = \frac{\mathrm{Re}}{M}$), are also instrumental in explaining the flow dynamics.

Our identified regimes include the following: stable slumping (low to moderate inclination angles, small density differences, low injection rates, high-yield stresses); unstable slumping (high injection rates, low to moderate inclination angles, small density differences,); separation (high inclination angles, significant density differences, large yield stresses, small to moderate injection rates, yield stresses); and mixing (high inclination angles, large density differences, low yield stresses, moderate to high injection rates). The stable-unstable slumping transition occurs at $\mathrm{Re}^* \approx 2800$, the slumping-separation transition at $\frac{\chi}{B} \approx 40$, and the separation-mixing transition at $\mathrm{Re}^* \approx -50\frac{\chi}{B} + 15\,000$. Also, mixing experiments are further classified into diffusive and nondiffusive subregimes using a new similarity scaling, where the transition between diffusive and nondiffusive occurs at $\mathrm{Re}^* \approx 5000$. In addition, interfacial velocities (front, separated piece, backflow front) correlate with inertial-buoyant stress balance. Our UDV analysis shows smooth positive and negative velocities in stable slumping, fluctuating velocities in unstable slumping, oscillating axial and negative velocities in separation, and complex irregular patterns in mixing. Also, the dynamic mixing index (MI) analysis reveals four stages: initial decrease, increase, subsequent decrease, and stabilization. Higher Re^* initially improves fluid placement but later diminishes it, while increasing χ/B consistently worsens it. The final mixing index (MI_f), i.e., when the heavy fluid front reaches the pipe end, correlates with χ, indicating that increased buoyancy amplifies instabilities and mixing.

Our research has provided detailed regime classifications and insights into the flow dynamics of buoyant miscible viscoplastic injections, the results of which can be relevant to P&A operations, 3D printing technology, etc. In fact, the understanding gained may enable control over various flow regimes and subregimes, by manipulating the flow parameters, e.g., the properties of *in situ* and injected fluids. Future work should further investigate the effects of the flow geometrical parameter (diameter ratios, eccentricity, and domain length) on the identified flow regimes and transitions. Future work should also focus on developing mathematical models to predict these regimes and subregimes, as well as conducting high-resolution computational studies on the flow characteristics in each flow regime.

The data supporting this study's findings are available within the article.

ACKNOWLEDGMENTS

This research has been carried out at the Université Laval. We gratefully acknowledge the financial support provided by PTAC-AUPRF through Grant No. AUPRF2022-000124 and NSERC (Natural Sciences and Engineering Research Council of Canada) through Alliance Grant No. ALLRP577111-22 ("Towards Net-Zero Emissions: Mechanics, processes and materials to support risk-based well decommissioning"). We also acknowledge the support provided by the Canada Foundation for Innovation (CFI) through the John R. Evans Leaders Fund (Grants No. GF130120, No. GQ130119, and No. GF525075), the Canada Research Chair (CRC) on Modeling Complex Flows (Grant No. CG125810), the NSERC Discovery Grant (Grant No. CG109154), and the NSERC Research Tools and Instruments Grant (Grant No. CG132931).

The authors report no conflict of interest.

[1] C. Duan, X. Yang, S. Jiang, C. Zhu, Y. Ma, and T. Fu, Early stage of externally driven filling of viscous fluids within a microfluidic pore-doublet network, Phys. Fluids **34**, 022001 (2022).
[2] P. D. Howell, S. L. Waters, and J. B. Grotberg, The propagation of a liquid bolus along a liquid-lined flexible tube, J. Fluid Mech. **406**, 309 (2000).
[3] S. Kar, S. S. Das, S. Laha, and S. Chakraborty, Microfluidics on porous substrates mediated by capillarity-driven transport, Ind. Eng. Chem. Res. **59**, 3644 (2020).
[4] I. Palabiyik, B. Olunloyo, P. J. Fryer, and P. T. Robbins, Flow regimes in the emptying of pipes filled with a Herschel–Bulkley fluid, Chem. Eng. Res. Des. **92**, 2201 (2014).
[5] I. Palabiyik, E. Lopez-Quiroga, P. T. Robbins, K. R. Goode, and P. Fryer, Removal of yield-stress fluids from pipework using water, AIChE J. **64**, 1517 (2018).
[6] J. Wiklund, M. Stading, and C. Trägårdh, Monitoring liquid displacement of model and industrial fluids in pipes by in-line ultrasonic rheometry, J. Food Eng. **99**, 330 (2010).
[7] S. K. Veerabhadrappa, J. J. Trivedi, and E. Kuru, Visual confirmation of the elasticity dependence of unstable secondary polymer floods, Ind. Eng. Chem. Res. **52**, 6234 (2013).
[8] P. Bazazi, H. A. Stone, and S. H. Hejazi, Spongy all-in-liquid materials by *in situ* formation of emulsions at oil-water interfaces, Nat. Commun. **13**, 4162 (2022).
[9] M. J. Shojaei, K. Osei-Bonsu, P. Grassia, and N. Shokri, Foam flow investigation in 3D-printed porous media: Fingering and gravitational effects, Ind. Eng. Chem. Res. **57**, 7275 (2018).
[10] L. Wang, Y. Zhang, R. Zou, R. Zou, L. Huang, Y. Liu, Z. Meng, Z. Wang, and H. Lei, A systematic review of CO_2 injection for enhanced oil recovery and carbon storage in shale reservoirs, Int. J. Hydrogen Energy **48**, 37134 (2023).
[11] C. Zhang, E. Wang, B. Li, X. Kong, J. Xu, S. Peng, and Y. Chen, Laboratory experiments of CO_2-enhanced coalbed methane recovery considering CO_2 sequestration in a coal seam, Energy **262**, 125473 (2023).
[12] M. Faramarzi-Palangar and A. Mirzaei-Paiaman, Identifying two-phase flow rock types in CO_2-brine systems using TEM-function, J. Pet. Sci. Eng. **205**, 108818 (2021).
[13] S. Akbari and S. M. Taghavi, Fluid experiments on the dump bailing method in the plug and abandonment of oil and gas wells, J. Pet. Sci. Eng. **205**, 108920 (2021).
[14] T. Zhang, M. Tang, Y. Ma, G. Zhu, Q. Zhang, J. Wu, and Z. Xie, Experimental study on CO_2/water flooding mechanism and oil recovery in ultralow-permeability sandstone with online LF-NMR, Energy **252**, 123948 (2022).
[15] A. Maleki and I. A. Frigaard, Turbulent displacement flows in primary cementing of oil and gas wells, Phys. Fluids **30**, 123101 (2018).
[16] R. Karyappa, A. Ohno, and M. Hashimoto, Immersion precipitation 3D printing (IP 3DP), Mater. Horiz. **6**, 1834 (2019).
[17] S. Lawson, X. Li, H. Thakkar, A. A. Rownaghi, and F. Rezaei, Recent advances in 3D printing of structured materials for adsorption and catalysis applications, Chem. Rev. **121**, 6246 (2021).
[18] J. van der Kolk, D. Tieman, and M. Jalaal, Viscoplastic lines: Printing a single filament of yield stress material on a surface, J. Fluid Mech. **958**, A34 (2023).
[19] N. Louvet, D. Bonn, and H. Kellay, Nonuniversality in the pinch-off of yield stress fluids: Role of nonlocal rheology, Phys. Rev. Lett. **113**, 218302 (2014).
[20] D. Lohse, Fundamental fluid dynamics challenges in inkjet printing, Annu. Rev. Fluid Mech. **54**, 349 (2022).
[21] M. Khalifeh and A. Saasen, *Introduction to Permanent Plug and Abandonment of Wells* (Springer Nature, Berlin, 2020).
[22] S. Akbari and S. M. Taghavi, From breakup to coiling and buckling regimes in buoyant viscoplastic injections, J. Fluid Mech. **940**, A42 (2022).
[23] M. Pourjafar-Chelikdani, A. Lavaf, B. Taghilou, S. Almasi, S. Kowsar, H. Najafi-Astmal, A. Mahdavi Nejad, and K. Sadeghy, On the use of viscous micropumps for the transport of yield-stress liquids in microfluidic systems, J. Non-Newtonian Fluid Mech. **308**, 104894 (2022).
[24] E. Chaparian, C. E. Owens, and G. H. McKinley, Computational rheometry of yielding and viscoplastic flow in vane-and-cup rheometer fixtures, J. Non-Newtonian Fluid Mech. **307**, 104857 (2022).

[25] D. Bonn, M. M. Denn, L. Berthier, T. Divoux, and S. Manneville, Yield stress materials in soft condensed matter, Rev. Mod. Phys. **89**, 035005 (2017).
[26] I. A. Frigaard, Simple yield stress fluids, Curr. Opin. Colloid Interface Sci. **43**, 80 (2019).
[27] P. Coussot and F. Gaulard, Gravity flow instability of viscoplastic materials: The ketchup drip, Phys. Rev. E **72**, 031409 (2005).
[28] N. J. Balmforth, N. Dubash, and A. C. Slim, Extensional dynamics of viscoplastic filaments: I. Long-wave approximation and the Rayleigh instability, J. Non-Newtonian Fluid Mech. **165**, 1139 (2010).
[29] N. J. Balmforth, N. Dubash, and A. C. Slim, Extensional dynamics of viscoplastic filaments: II. Drips and bridges, J. Non-Newtonian Fluid Mech. **165**, 1147 (2010).
[30] M. Aytouna, J. Paredes, N. Shahidzadeh-Bonn, S. Moulinet, C. Wagner, Y. Amarouchene, J. Eggers, and D. Bonn, Drop formation in non-Newtonian fluids, Phys. Rev. Lett. **110**, 034501 (2013).
[31] A. Geffrault, H. Bessaies-Bey, N. Roussel, and P. Coussot, Extensional gravity-rheometry (EGR) for yield stress fluids, J. Rheol. **65**, 887 (2021).
[32] P. Moschopoulos, A. Syrakos, Y. Dimakopoulos, and J. Tsamopoulos, Dynamics of viscoplastic filament stretching, J. Non-Newtonian Fluid Mech. **284**, 104371 (2020).
[33] R. Valette, E. Hachem, M. Khalloufi, A. S. Pereira, M. R. Mackley, and S. A. Butler, The effect of viscosity, yield stress, and surface tension on the deformation and breakup profiles of fluid filaments stretched at very high velocities, J. Non-Newtonian Fluid Mech. **263**, 130 (2019).
[34] M. Jalaal, B. Stoeber, and N. J. Balmforth, Spreading of viscoplastic droplets, J. Fluid Mech. **914**, A21 (2021).
[35] H. K. Zhang, Y. R. Yin, X. M. Zhang, S. C. Chen, W. X. Chen, and G. H. Hu, Numerical simulation of the hydrodynamics of yield stress fluids during dip coating, J. Non-Newtonian Fluid Mech. **298**, 104675 (2021).
[36] M. Jalaal, Controlled spreading of complex droplets, Ph.D. thesis, University of British Columbia, 2016.
[37] A. Saïdi, C. Martin, and A. Magnin, Influence of yield stress on the fluid droplet impact control, J. Non-Newtonian Fluid Mech. **165**, 596 (2010).
[38] A. Amiri, A. Eslami, R. Mollaabbasi, F. Larachi, and S. M. Taghavi, Removal of a yield stress fluid by a heavier Newtonian fluid in a vertical pipe, J. Non-Newtonian Fluid Mech. **268**, 81 (2019).
[39] H. Hassanzadeh, I. A. Frigaard, and S. M. Taghavi, Neutrally buoyant miscible jets into viscoplastic ambient fluids, J. Non-Newtonian Fluid Mech. **320**, 105107 (2023).
[40] S. Akbari and S. M. Taghavi, Immersed buoyant viscoplastic injections, J. Non-Newtonian Fluid Mech. **306**, 104836 (2022).
[41] S. Lyu and S. M. Taghavi, Viscoplastic displacements in axially rotating pipes, J. Non-Newtonian Fluid Mech. **284**, 104353 (2020).
[42] S. M. Taghavi, Displacement flows in rotating pipes, Sci. Talks **3**, 100066 (2022).
[43] A. Renteria and I. A. Frigaard, Primary cementing of horizontal wells. Displacement flows in eccentric horizontal annuli. Part 1. Experiments, J. Fluid Mech. **905**, A7 (2020).
[44] R. Mollaabbasi, S. Noroozi, F. Larachi, and S. M. Taghavi, Efficient displacement of fluids using a viscous shear-thinning spacer, Ind. Eng. Chem. Res. **60**, 10376 (2021).
[45] S. M. Taghavi, K. Alba, M. Moyers-Gonzalez, and I. A. Frigaard, Incomplete fluid–fluid displacement of yield stress fluids in near-horizontal pipes: Experiments and theory, J. Non-Newtonian Fluid Mech. **167-168**, 59 (2012).
[46] K. Alba, S. M. Taghavi, J. R. de Bruyn, and I. A. Frigaard, Incomplete fluid–fluid displacement of yield-stress fluids. Part 2: Highly inclined pipes, J. Non-Newtonian Fluid Mech. **201**, 80 (2013).
[47] A. Bougouin and L. Lacaze, From inertial to viscous slumping: Numerical and experimental insights of a transient intermediate regime, Phys. Rev. Fluids **7**, 094803 (2022).
[48] M. Moyers-Gonzalez, J. N. Hewett, D. R. Cusack, B. M. Kennedy, and M. Sellier, Non-isothermal thin-film flow of a viscoplastic material over topography: Critical Bingham number for a partial slump, Theor. Comput. Fluid Dyn. **37**, 151 (2023).
[49] E. M. Hinton and A. J. Hogg, Flow of a yield-stress fluid past a topographical feature, J. Non-Newtonian Fluid Mech. **299**, 104696 (2022).

[50] C. Gadal, M. J. Mercier, M. Rastello, and L. Lacaze, Slumping regime in lock-release turbidity currents, J. Fluid Mech. **974**, A4 (2023).
[51] D. Sher and A. W. Woods, Mixing in continuous gravity currents, J. Fluid Mech. **818**, R4 (2017).
[52] S. M. Taghavi, T. Séon, D. M. Martinez, and I. A. Frigaard, Influence of an imposed flow on the stability of a gravity current in a near horizontal duct, Phys. Fluids **22**, 031702 (2010).
[53] K. Alba, S. M. Taghavi, and I. A. Frigaard, Miscible density unstable displacement flows in inclined tube, Phys. Fluids **25**, 067101 (2013).
[54] A. Amiri, F. Larachi, and S. M. Taghavi, Buoyant miscible displacement flows in vertical pipe, Phys. Fluids **28**, 102105 (2016).
[55] S. Akbari and S. M. Taghavi, Injection of a heavy fluid into a light fluid in a closed-end pipe, Phys. Fluids **32**, 063302 (2020).
[56] S. Akbari and S. M. Taghavi, Buoyant fluid injections at high viscosity contrasts in an inclined closed-end pipe, Phys. Fluids **35**, 022102 (2023).
[57] K. Alba and I. A. Frigaard, Dynamics of the removal of viscoplastic fluids from inclined pipes, J. Non-Newtonian Fluid Mech. **229**, 43 (2016).
[58] S. M. Taghavi, T. Séon, K. Wielage-Burchard, D. M. Martinez, and I. A. Frigaard, Stationary residual layers in buoyant Newtonian displacement flows, Phys. Fluids **23**, 044105 (2011).
[59] K. Alba, S. M. Taghavi, and I. A. Frigaard, Miscible heavy light displacement flows in an inclined two dimensional channel: A numerical approach, Phys. Fluids **26**, 122104 (2014).
[60] K. C. Sahu, H. Ding, P. Valluri, and O. K. Matar, Pressure-driven miscible two-fluid channel flow with density gradients, Phys. Fluids **21**, 043603 (2009).
[61] R. Mollaabbasi and S. M. Taghavi, Buoyant displacement flows in slightly non uniform channels, J. Fluid Mech. **795**, 876 (2016).
[62] A. Dahi Taleghani and L. Santos, Well plugging and abandonment, *Wellbore Integrity: From Theory to Practice* (Springer, Berlin, 2023).
[63] E. B. Nelson and D. Guillot, *Well Cementing*, 2nd ed. (Schlumberger Educational Services, 2006).
[64] M. Bizhani and I. A. Frigaard, Buoyancy effects on turbulent displacement of viscoplastic fluids from strongly eccentric horizontal annuli, Phys. Fluids **32**, 125112 (2020).
[65] M. Bizhani, Y. Foolad, and I. A. Frigaard, Turbulent displacement flow of viscoplastic fluids in eccentric annulus: Experiments, Phys. Fluids **32**, 045117 (2020).
[66] M. Jalaal, D. Kemper, and D. Lohse, Viscoplastic water entry, J. Fluid Mech. **864**, 596 (2019).
[67] M. Zare and I. A. Frigaard, Onset of miscible and immiscible fluids' invasion into a viscoplastic fluid, Phys. Fluids **30**, 063101 (2018).
[68] N. Kazemi, S. Akbari, D. Vidal, and S. M. Taghavi, Buoyant miscible viscoplastic displacements in vertical pipes: Flow regimes and their characterizations, Phys. Fluids **36**, 012119 (2024).
[69] C. Y. Chen and E. Meiburg, Miscible displacements in capillary tubes. Part 2. Numerical simulations, J. Fluid Mech. **326**, 57 (1996).
[70] P. Petitjeans and T. Maxworthy, Miscible displacements in capillary tubes. Part 1. Experiments, J. Fluid Mech. **326**, 37 (1996).
[71] B. Eslami, S. Shariatnia, H. Ghasemi, and K. Alba, Non-isothermal buoyancy-driven exchange flows in inclined pipes, Phys. Fluids **29**, 062108 (2017).
[72] M. Habibi, M. Dinkgreve, J. Paredes, M. M. Denn, and D. Bonn, Normal stress measurement in foams and emulsions in the presence of slip, J. Non-Newtonian Fluid Mech. **238**, 33 (2016).
[73] R. S. Mitishita, J. A. MacKenzie, G. J. Elfring, and I. A. Frigaard, Fully turbulent flows of viscoplastic fluids in a rectangular duct, J. Non-Newtonian Fluid Mech. **293**, 104570 (2021).
[74] Z. Jaworski, T. Spychaj, A. Story, and G. Story, Carbomer microgels as model yield-stress fluids, Rev. Chem. Eng. **38**, 881 (2022).
[75] G. Ovarlez and S. Hormozi, *Lectures on visco-plastic fluid mechanics* (Springer, Berlin, 2019).
[76] A. Jain, R. Singh, L. Kushwaha, V. Shankar, and Y. M. Joshi, Role of inertia and thixotropy in start-up flows of aging soft materials: Transient dynamics and shear banding in a rate-controlled flow field, J. Rheol. **62**, 1001 (2018).

[77] A. Karppinen, T. Saarinen, J. Salmela, A. Laukkanen, M. Nuopponen, and J. Seppälä, Flocculation of microfibrillated cellulose in shear flow, Cellulose **19**, 1807 (2012).
[78] J. J. Griebler and S. A. Rogers, The nonlinear rheology of complex yield stress foods, Phys. Fluids **34**, 023107 (2022).
[79] M. Dinkgreve, J. Paredes, M. M. Denn, and D. Bonn, On different ways of measuring the yield stress, J. Non-Newtonian Fluid Mech. **238**, 233 (2016).
[80] G. J. Donley, J. R. de Bruyn, G. H. McKinley, and S. A. Rogers, Time-resolved dynamics of the yielding transition in soft materials, J. Non-Newtonian Fluid Mech. **264**, 117 (2019).
[81] A. Corker, H. C. H. Ng, R. J. Poole, and E. García-Tuñón, 3D printing with 2D colloids: Designing rheology protocols to predict printability of soft-materials, Soft Matter **15**, 1444 (2019).
[82] R. R. Fernandes, D. E. Andrade, A. T. Franco, and C. O. R. Negrão, The yielding and the linear-to-nonlinear viscoelastic transition of an elastoviscoplastic material, J. Rheol. **61**, 893 (2017).
[83] P. R. Varges, B. S. Fonseca, C. M. Costa, M. F. Naccache, P. R. de Souza Mendes, and H. A. Pinho, Exchange flows between yield stress materials and Newtonian oils, J. Non-Newtonian Fluid Mech. **261**, 123 (2018).
[84] P. J. T. Espinoza, P. R. Varges, E. C. Rodrigues, M. F. Naccache, and P. R. de Souza Mendes, Displacement flow of yield stress materials in annular spaces of variable cross section, J. Pet. Sci. Eng. **208**, 109614 (2022).
[85] A. Pourzahedi, M. Zare, and I. A. Frigaard, Eliminating injection and memory effects in bubble rise experiments within yield stress fluids, J. Non-Newtonian Fluid Mech. **292**, 104531 (2021).
[86] M. E. Villalba, M. Daneshi, E. Chaparian, and D. M. Martinez, Atypical plug formation in internal elastoviscoplastic fluid flows over non-smooth topologies, J. Non-Newtonian Fluid Mech. **319**, 105078 (2023).
[87] M. Daneshi, J. MacKenzie, N. J. Balmforth, D. M. Martinez, and D. R. Hewitt, Obstructed viscoplastic flow in a Hele-Shaw cell, Phys. Rev. Fluids **5**, 013301 (2020).
[88] Y. J. García-Blanco, V. Y. Urazaki, A. D. J. Rivera, L. H. Quitian, E. M. Germer, and A. T. Franco, Rheological characterization of viscoplastic fluid flow in a pipe with wall slip using *in situ* particle image velocimetry, Rheol. Acta **62**, 93 (2023).
[89] S. Kumar and S. N. Upadhyay, Laminar flow dissolution and diffusion in non-Newtonian fluid, Ind. Eng. Chem. Fund. **19**, 75 (1980).
[90] L. Jørgensen, M. Le Merrer, H. Delanoë-Ayari, and C. Barentin, Yield stress and elasticity influence on surface tension measurements, Soft Matter **11**, 5111 (2015).
[91] J. Boujlel and P. Coussot, Measuring the surface tension of yield stress fluids, Soft Matter **9**, 5898 (2013).
[92] A. Ghazal and I. Karimfazli, On the hydrodynamics of off-bottom plug placement: Effects of geometry in a 2D model problem, J. Pet. Sci. Eng. **212**, 110153 (2022).
[93] J. Sun, L. Guo, J. Fu, J. Jing, X. Yin, Y. Lu, A. Ullmann, and N. Brauner, A new model for viscous oil-water eccentric core annular flow in horizontal pipes, Int. J. Multiphase Flow **147**, 103892 (2022).
[94] E. I. Housz, G. Ooms, R. Henkes, M. Pourquie, A. Kidess, and R. Radhakrishnan, A comparison between numerical predictions and experimental results for horizontal core-annular flow with a turbulent annulus, Int. J. Multiphase Flow **95**, 271 (2017).
[95] K. C. Sahu, A new linearly unstable mode in the core-annular flow of two immiscible fluids, J. Fluid Mech. **918**, A11 (2021).
[96] L. Milton-McGurk, N. Williamson, S. W. Armfield, M. P. Kirkpatrick, and K. M. Talluru, Entrainment and structure of negatively buoyant jets, J. Fluid Mech. **911**, A21 (2021).
[97] L. Milton-McGurk, N. Williamson, S. W. Armfield, and M. P. Kirkpatrick, Characterising entrainment in fountains and negatively buoyant jets, J. Fluid Mech. **939**, A29 (2022).
[98] C. Toupoint, P. Ern, and V. Roig, Kinematics and wake of freely falling cylinders at moderate Reynolds numbers, J. Fluid Mech. **866**, 82 (2019).
[99] M. Debacq, V. Fanguet, J. P. Hulin, D. Salin, and B. Perrin, Self-similar concentration profiles in buoyant mixing of miscible fluids in a vertical tube, Phys. Fluids **13**, 3097 (2001).
[100] M. Debacq, J. P. Hulin, D. Salin, B. Perrin, and E. J. Hinch, Buoyant mixing of miscible fluids of varying viscosities in vertical tubes, Phys. Fluids **15**, 3846 (2003).

[101] T. Séon, J. Znaien, B. Perrin, E. J. Hinch, D. Salin, and J. P. Hulin, Front dynamics and macroscopic diffusion in buoyant mixing in a tilted tube, Phys. Fluids **19**, 125105 (2007).
[102] See Supplemental Material at http://link.aps.org/supplemental/10.1103/PhysRevFluids.9.073301 for a better visualization of the flow regimes identified in this study. The material includes four videos corresponding to stable slumping, unstable slumping, separation, and mixing flow regimes.
[103] T. Séon, J. P. Hulin, D. Salin, B. Perrin, and E. J. Hinch, Buoyant mixing of miscible fluids in tilted tubes, Phys. Fluids **16**, L103 (2004).
[104] T. Séon, J. P. Hulin, D. Salin, B. Perrin, and E. J. Hinch, Laser-induced fluorescence measurements of buoyancy driven mixing in tilted tubes, Phys. Fluids **18**, 041701 (2006).
[105] A. Amiri, F. Larachi, and S. M. Taghavi, Displacement flows in periodically moving pipe: Understanding multiphase flows hosted in oscillating geometry, Chem. Eng. Sci. **170**, 437 (2017).
[106] T. Séon, J. P. Hulin, D. Salin, B. Perrin, and E. J. Hinch, Buoyancy driven miscible front dynamics in tilted tubes, Phys. Fluids **17**, 031702 (2005).
[107] L. H. Carnevale, P. Deuar, Z. Che, and P. E. Theodorakis, Liquid thread breakup and the formation of satellite droplets, Phys. Fluids **35**, 074108 (2023).
[108] X. Chen, A. P. O'Mahony, and T. Barber, Experimental study of the stable droplet formation process during micro-valve-based three-dimensional bioprinting, Phys. Fluids **35**, 011903 (2023).
[109] L. Liu, H. Wang, C. Zhu, Y. Ma, and T. Fu, Fragmentation of asymmetric liquid filaments and formation of satellite droplets in a microchannel, Int. J. Multiphase Flow **158**, 104290 (2023).
[110] H. Jiang, G. Wang, C. Zhu, T. Fu, and Y. Ma, Dynamics of droplet formation and mechanisms of satellite droplet formation in T-junction microchannel, Chem. Eng. Sci. **248**, 117217 (2022).
[111] P. Kumari and A. Atta, Insights into the dynamics of non-Newtonian droplet formation in a T-junction microchannel, Phys. Fluids **34**, 062001 (2022).
[112] J. Suckale, Z. Qin, D. Picchi, T. Keller, and I. Battiato, Bistability of buoyancy-driven exchange flows in vertical tubes, J. Fluid Mech. **850**, 525 (2018).
[113] M. S. Salehi, M. T. Esfidani, H. Afshin, and B. Firoozabadi, Experimental investigation and comparison of Newtonian and non-Newtonian shear-thinning drop formation, Exp. Therm. Fluid Sci. **94**, 148 (2018).
[114] A. Haider and O. Levenspiel, Drag coefficient and terminal velocity of spherical and nonspherical particles, Powder Technol. **58**, 63 (1989).
[115] F. Altuhafi, C. O'Sullivan, and I. Cavarretta, Analysis of an image-based method to quantify the size and shape of sand particles, J. Geotech. Geoenviron. Eng. **139**, 1290 (2013).
[116] J. Rodriguez, J. Johansson, and T. Edeskär, Particle shape determination by two-dimensional image analysis in geotechnical engineering, in *Proceedings of the Nordic Geotechnical Meeting* (Danish Geotechnical Society, Lyngby, Denmark, 2012), pp. 207–218.
[117] J. Zheng and R. D. Hryciw, Traditional soil particle sphericity, roundness and surface roughness by computational geometry, Géotechnique **65**, 494 (2015).
[118] W. C. Krumbein and L. L. Sloss, *Stratigraphy and Sedimentation* (Soil Science, Philadelphia, USA, 1951), Vol. 71.
[119] Z. Huang, G. Lin, and A. Ardekani, Consistent, essentially conservative and balanced-force phase-field method to model incompressible two-phase flows, J. Comput. Phys. **406**, 109192 (2020).